

TECHNISCHE UNIVERSITÄT MÜNCHEN

DEPARTMENT OF PHYSICS

BACHELOR'S THESIS IN PHYSICS

Limits on Astrophysical Neutrino Emission from IceCube Alert Positions

Author

Anna Magdalena SCHUBERT

Supervisor

Prof. Elisa RESCONI

28th July 2020



Abstract

This thesis presents the upper flux limits with 90% confidence for 79 IceCube high-energy neutrino alert event positions. P-value, sensitivity and 3σ discovery potential are calculated for every position as a reproduction of a previous work by the author of [23]. The p-values are calculated without trial correction. The analysis method is a time-independent point-source search using an unbinned likelihood approach. The unblinded data as well as the background trials and the simulated signal trials are provided by the author of [23].

The analysis is first performed for all positions individually. For 13 candidate positions the 3σ discovery potential lies between the sensitivity and the flux limit. They are therefore the most interesting candidates for further investigations. The most significant single source at RA 111.36° and DEC -0.37° has a p-value of 0.022 and a flux limit of $7.144 \cdot 10^{-13} \frac{\text{TeV}}{\text{cm}^2\text{s}}$.

The individual analysis is followed by two stacking analyses: \mathcal{TS} value and p-value stacking. The \mathcal{TS} value stacking results in a p-value of 0.8171 and the \mathcal{TS} stacked flux limit is constrained to $6.74 \cdot 10^{-12} \frac{\text{TeV}}{\text{cm}^2\text{s}}$. The p-value stacking results in a p-value of 0.8261 and the p-value stacked flux limit is constrained to $6.54 \cdot 10^{-12} \frac{\text{TeV}}{\text{cm}^2\text{s}}$.

The individual analysis was first performed assuming an elliptic error region. When a rectangular error region is used instead, most of the flux limits are slightly higher due to increasing background fluctuations. For few positions a considerably higher flux limit obtained using the larger rectangular error region indicates a possible source outside the assumed elliptic error region. For EHE28 at RA 99.0° and DEC -15.02° the p-value decreased from 0.987 to 0.147 when the rectangular error region is used instead of the elliptic one. The flux limit $\Phi_{90\%}$ assuming the rectangular shape is $2.847 \cdot 10^{-12} \frac{\text{TeV}}{\text{cm}^2\text{s}}$ for this position.

The individual flux limits are compared to the flux limits of a source catalog, calculated by the IceCube collaboration. Both flux limit sets show similar results and follow the same course depending on the declination.

Contents

1	Introduction	1
2	Neutrino physics	3
2.1	Neutrino properties	3
2.1.1	Historical overview	3
2.1.2	Neutrino masses	3
2.1.3	Neutrino interactions with matter	4
2.2	High-energy neutrino astronomy	5
2.2.1	Generation of astrophysical neutrinos	6
2.2.2	Astrophysical neutrino sources	8
2.2.3	Atmospheric neutrino background	9
3	Point-source search in IceCube	11
3.1	The IceCube Neutrino Observatory	11
3.1.1	Functional description of the detector	12
3.1.2	Data acquisition and filtering	12
3.2	High-energy neutrino events	13
3.2.1	Event topologies	14
3.2.2	Event reconstruction	14
3.2.3	Event selection	17
3.3	Point-source search method	18
3.3.1	Unbinned likelihood ratio	18
3.3.2	Signal and background PDFs	19
4	Point-source search for neutrino excess from alert positions	21
4.1	Analysis approach	22
4.1.1	Position fit	22
4.1.2	Trial generation	23
4.1.3	Unit conversion	24

4.2	Sensitivity and discovery potential	24
4.2.1	Analysis method	24
4.2.2	Sensitivity	25
4.2.3	Discovery potential	26
4.3	P-values	27
5	Upper limits on astrophysical neutrino emission	29
5.1	Individual analysis	30
5.2	Stacked analysis	35
5.2.1	\mathcal{TS} value stacking	35
5.2.2	P-value stacking	37
5.2.3	Stacking results and comparison	39
5.3	Variation of considered error region	40
5.4	Comparison to limits of source catalog	42
6	Conclusion and outlook	43

List of Figures

2.1	Deep inelastic neutrino-nucleus scattering	5
2.2	Neutrino universe at high energies	6
2.3	Multi-messenger astronomy overview	7
2.4	Active galactic nucleus	8
2.5	Neutrino spectra for atmospheric and astrophysical neutrinos	10
3.1	Illustration of the IceCube detector	11
3.2	Cherenkov radiation	12
3.3	Event topologies in IceCube	13
3.4	Track reconstruction	16
3.5	Neutrino absorption in Earth	17
4.1	Skymap with high-energy alert event positions and error regions	21
4.2	Position fits	22
4.3	Background and signal \mathcal{TS} distributions	23
4.4	Analysis method for sensitivity and discovery potential	25
4.5	Illustration of sensitivity and discovery potential	26
4.6	Declination dependency of sensitivity and discovery potential	27
4.7	P-value calculation	28
5.1	Illustration of upper flux limit	29
5.2	Correlation of upper flux limit with declination and error region	30
5.3	Skymap with most significant positions	31
5.4	Stacked data distributions	35
5.5	TS value stacking	36
5.6	P-value stacking	38
5.7	Effects of variation of error region	40
5.8	Comparison to limits of source catalog	42

List of Tables

1	Results for AHES events	32
2	Results for EHE events	33
3	Results for DIF events	34
4	Stacking results	39
5	Results for rectangular error region	41

1 Introduction

Multi-messenger astronomy exploits the synergy of astrophysical messengers such as photons, cosmic rays and neutrinos. Photons provide information e.g. on the surface, temperature and spectra of possible multi-messenger sources, while cosmic rays for example grant additional insight into the acceleration processes [4]. Neutrinos are assumed to be produced in processes that produce also cosmic rays. Contrary to γ -rays and cosmic rays, neutrinos travel from their sources towards Earth almost without deflection or absorption, because they hardly interact with matter and do not interact with electromagnetic fields. Therefore neutrinos can be used as tracers that point back to multi-messenger sources. Due to their very low interaction probability neutrinos are however hard to detect and observatories with an immense detection volume are required. One of the currently best equipped detectors is the IceCube detector, located at the geographic South Pole.

Even though the interest in astrophysical neutrinos emerged from cosmic ray researches, it is also individually a promising field. In 2017 an IceCube high-energy neutrino alert was coincident with a γ -ray flare from the blazar TXS 0506+056. This motivated a detailed analysis of the neutrino emission from the blazar's position and led to the observation of an astrophysical neutrino excess [6]. This observation motivated a search for astrophysical neutrino emission at the positions of all IceCube high-energy neutrino alerts, which is presented in the following.

This thesis provides an overview of neutrino physics (chapter 2) and neutrino detection with the IceCube detector (chapter 3). After a detailed explanation of the analysis approach (chapter 4) the main interest is the calculation of the upper flux limits with 90% confidence for 79 of the IceCube high-energy neutrino alert positions (chapter 5). The analysis is first performed for every position individually followed by a \mathcal{TS} -value and a p-value stacked analysis. In the end the effect of a variation of the considered error region is discussed and the limit results are compared to the flux limits for a source catalog, presented in [14].

2 Neutrino physics

This chapter provides information on the physical properties of neutrinos. Those are necessary to understand the functionality of the IceCube detector and the analysis presented in this work. Besides the explanation of the neutrino's role in the standard model and its interactions, an overview of neutrinos and their role in high-energy multi-messenger astronomy is given.

2.1 Neutrino properties

As a part of the standard model of particle physics, neutrinos are electrically uncharged leptons (spin $\frac{1}{2}$) which interact mainly via weak interactions. There are three known lepton families, each containing a charged lepton and its corresponding neutrino [26]:

$$\begin{pmatrix} \nu_e \\ e^- \end{pmatrix} \begin{pmatrix} \nu_\mu \\ \mu^- \end{pmatrix} \begin{pmatrix} \nu_\tau \\ \tau^- \end{pmatrix}$$

2.1.1 Historical overview

The neutrino was firstly postulated by Wolfgang Pauli in 1930 to make the β -decay consistent with the conservation of energy, momentum and angular momentum. Thereupon, a theory describing the phenomenon was presented by Enrico Fermi so that the β -decay is expressed as [20]

$$n \rightarrow p^+ + e^- + \bar{\nu}_e. \quad (2.1)$$

The first actual detection of neutrinos was the detection of electron anti-neutrinos by Clyde L. Cowan and Frederick Reines in 1956. [26]

2.1.2 Neutrino masses

One of the fundamental questions of neutrino research is their mass. To answer this, it is necessary to go beyond the standard model: It predicts neutrinos to be massless but neutrino flavor oscillation observations established a non-zero neutrino mass. This was proven by the observation of neutrinos changing flavor by the Super-Kamiokande collaboration, presented in 1998 in Takayama [29].

The three neutrino flavor states $|\nu_{e,\mu,\tau}\rangle$ do not directly correspond to the three mass states $|\nu_{1,2,3}\rangle$. Each neutrino flavor state can instead be understood as a quantum mechanical linear combination of mass states:

$$\begin{pmatrix} |\nu_e\rangle \\ |\nu_\mu\rangle \\ |\nu_\tau\rangle \end{pmatrix} = \begin{pmatrix} U_{e1} & U_{e2} & U_{e3} \\ U_{\mu1} & U_{\mu2} & U_{\mu3} \\ U_{\tau1} & U_{\tau2} & U_{\tau3} \end{pmatrix} \cdot \begin{pmatrix} |\nu_1\rangle \\ |\nu_2\rangle \\ |\nu_3\rangle \end{pmatrix} \quad (2.2)$$

The leptonic 3 x 3 mixing matrix U , the PMNS-matrix, short for Pontecorvo-Maki-Nakagawa-Sakata matrix, is unitary and contains three mixing angles as well as one phase. The relative phases of the mass eigenstates change with time, which makes it impossible for neutrinos to have no mass or equal mass for each flavor. [26]

Because neutrinos do have a mass, even though it is very small, they also underlie the gravitational force. This makes them possible dark matter candidates [5].

2.1.3 Neutrino interactions with matter

The two main weak interaction processes of neutrinos are neutral current and charged current processes. The cosmic neutrinos detected in IceCube have energies above 100 GeV. They interact with nuclei in the ice via deep inelastic scattering.

Neutral current

In neutral current processes a neutrino ν_l with flavor l interacts with a nucleon N , exchanging an uncharged Z^0 -boson. The involved lepton remains unchanged and a hadronic cascade N^* can be generated:

$$\nu_l + N \rightarrow \nu_l + N^* \quad (2.3)$$

Charged current

In charged current processes the interaction is mediated by a charged W^\pm boson and the kind of the involved lepton changes. In contrast to neutral current processes, the outgoing particle is a charged lepton l which can be detected (cf. chapter 3):

$$\nu_l + N \rightarrow l + N^* \quad (2.4)$$

There are three sub-types of charged current interactions, depending on the neutrino energy. The one relevant for neutrino detection in IceCube is the last one. [26, 18, 22]

- For neutrino energies below ~ 0.1 GeV the nucleus is assumed to be point-like, hence the process can be described as quasi-elastic scattering.

- For neutrino energies between ~ 0.1 GeV and 20 GeV the potential production of pions and kaons due to resonant baryonic excitations of the nucleus have to be taken into account.
- For neutrino energies above 20 GeV, deep inelastic scattering is taking place, because of the neutrino's effect on the quark structure of the nucleus. The Feynman diagram for a muon-neutrino deep inelastic scattering is shown in figure 2.1.

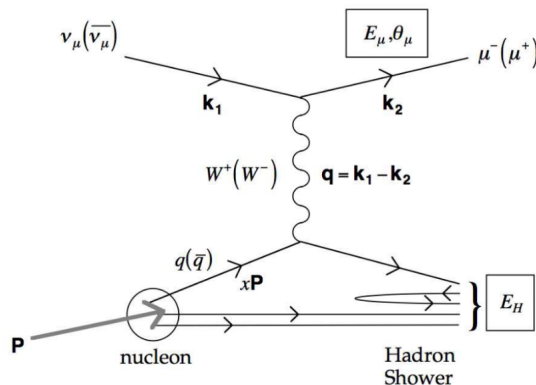


Figure 2.1: Charged current process of a muon-neutrino nucleus deep inelastic scattering. The muon neutrino interacts with the nucleus via exchange of a W^\pm boson. The outgoing muon can be detected. A hadronic cascade is produced. Figure taken from [18].

2.2 High-energy neutrino astronomy

Neutrinos are uncharged leptons that do not underlie the electromagnetic force. Therefore they have a very small cross section, compared to photons or charged particles. This allows them to propagate through the universe almost without deflection and cosmic neutrinos that reach the Earth point almost directly back to their source. This makes neutrinos highly informative messenger particles. The visible range for γ -rays decreases rapidly for high energies because of absorption. Charged cosmic rays (CRs) still reach the Earth but they get deflected by magnetic fields and do not allow precise pointing. The universe at high energies and distances remains unobstructed only to neutrinos (cf. figure 2.2). On these grounds neutrinos are on the one hand predestined messengers for searches for astrophysical multi-messenger sources (AMS), but on the other hand very hard to detect (cf. chapter 3).

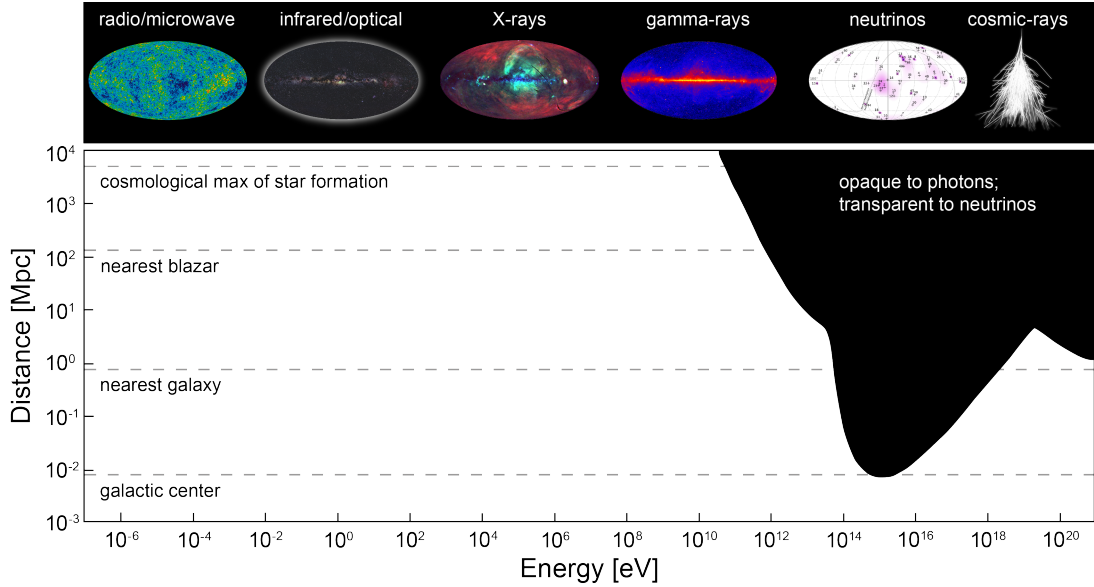


Figure 2.2: Energy spectrum vs. range of the explorable universe using different particles. The universe becomes at high energies opaque to photons but can still be explored with neutrinos. Figure taken from [1].

This chapter covers how astrophysical neutrinos are assumed to be generated and accelerated in AMS. It presents potential neutrino and cosmic ray sources and introduces atmospheric neutrinos, which are treated as background in the performed analysis.

2.2.1 Generation of astrophysical neutrinos

To understand possible ways of neutrino generation, cosmic rays have to be introduced. Cosmic rays are highly energetic protons and heavier ionized nuclei that travel through the universe with up to almost the speed of light. Underlying the electromagnetic force, cosmic rays get deflected in magnetic fields. Therefore they considerably lose their directional information.

Neutrinos can be produced when cosmic ray particles interact with ambient matter or photons near their acceleration site. Because neutrinos propagate almost without deflection, they can be used to investigate the location of cosmic ray sources. The directional behavior of cosmic rays, γ -rays and neutrinos is visualized in figure 2.3.

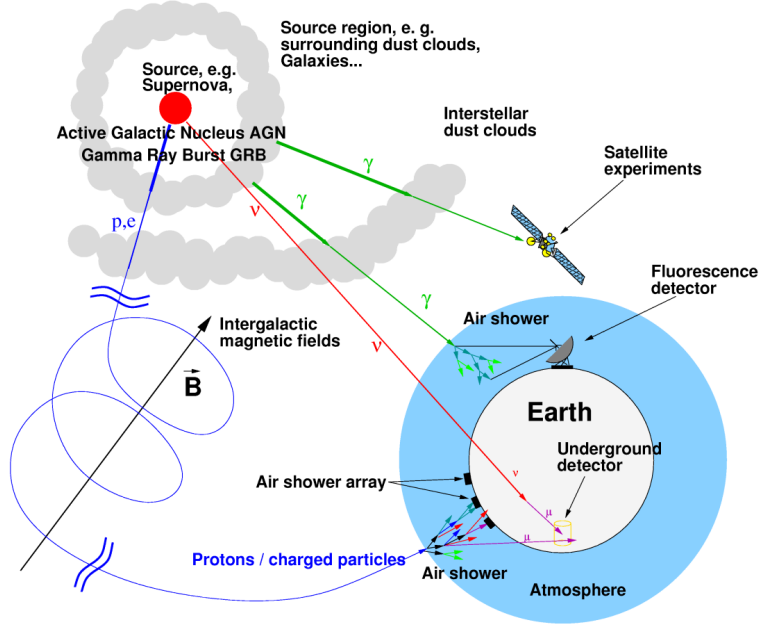


Figure 2.3: Visualization of different messenger particles emitted by an astrophysical source. Only neutrinos (red) reach Earth without deflection or absorption. When the neutrinos interact in the Earth they can produce leptons which then can be detected. Cosmic rays (blue) get deflected by magnetic fields and γ -rays (green) can be absorbed by dust clouds. Figure taken from [17].

The neutrino production proceeds via pion-productions in proton-photon or proton-proton interactions. The dominant reactions are the ones in equation 2.5 and 2.6. If the incident particle is a neutron instead of a proton, π^- particles are produced. Reaching higher energies, also the contribution of kaons to this spectrum occurs.

$$p\gamma \rightarrow \Delta^+ \rightarrow \begin{cases} p\pi^0, & \text{fraction } 2/3 \\ n\pi^+, & \text{fraction } 1/3 \end{cases} \quad (2.5)$$

$$pp \rightarrow \begin{cases} pp\pi^0, & \text{fraction } 2/3 \\ pn\pi^+, & \text{fraction } 1/3 \end{cases} \quad (2.6)$$

The produced neutrons are very likely to interact before decaying. The charged pions instead decay and produce neutrinos as secondary particles of cosmic rays:

$$\pi^+ \rightarrow \mu^+ \nu_\mu \rightarrow e^+ \nu_e \bar{\nu}_\mu \nu_\mu \quad (2.7)$$

$$\pi^- \rightarrow \mu^- \bar{\nu}_\mu \rightarrow e^- \bar{\nu}_e \nu_\mu \bar{\nu}_\mu \quad (2.8)$$

The neutrino flavor ratio of produced neutrinos in the presented processes is

$$(\nu_e : \nu_\mu : \nu_\tau)_{\text{source}} = (1 : 2 : 0) \quad (2.9)$$

Due to oscillation processes along their way towards Earth, explained in more detail in [4], it is expected, that the amount of neutrinos reaching Earth is equal for each flavor [4]:

$$(\nu_e : \nu_\mu : \nu_\tau)_{\text{Earth}} = (1 : 1 : 1) \quad (2.10)$$

2.2.2 Astrophysical neutrino sources

There are three distinguishable types of neutrinos: Neutrinos from extra-galactic sources, neutrinos from galactic sources and atmospheric neutrino background (cf. chapter 2.2.3). In this work the focus lies on extra-galactic sources. Two of the most promising candidates are the following:

Active galactic nuclei An active galactic nucleus (AGN) is a very luminous center of a galaxy. AGN emit a broad band from radio to $>\text{TeV}$ γ -rays and are strongly time-variant. Their extremely high energies make them potential sources of ultra-high energy cosmic particles. AGN are powered by the gravitational energy arising from a rotating super-massive black hole (BH) in the center of the galaxy. This hub is believed to be surrounded by an accretion disk and further by a thicker, opaque torus. Parallel to the spinning axis a relativistic jet can be formed. Depending on the angle of sight relative to the jet, AGN can be sub-classified. If one of the jets is for example orientated towards the observer, it is a so called blazar, which are promising AMS candidates. [19]; A schematic view of an AGN is shown in figure 2.4.

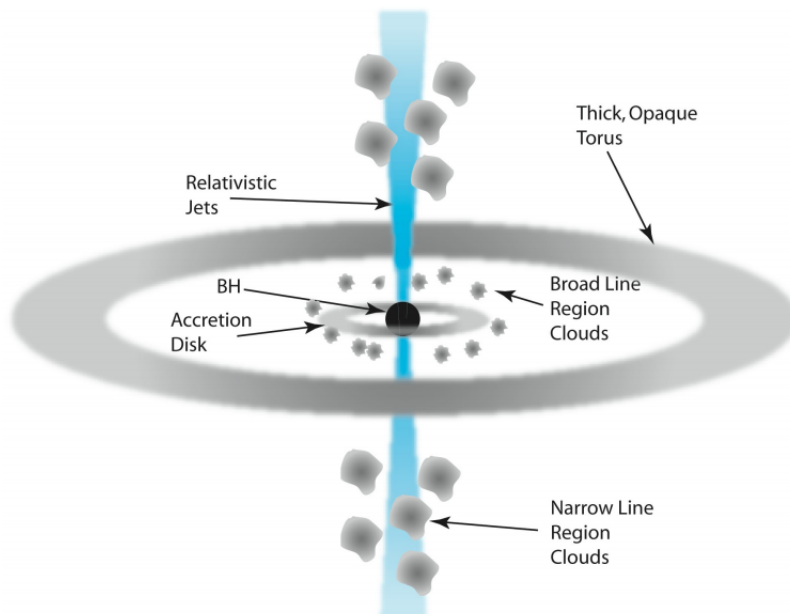


Figure 2.4: Schematic view of an active galactic nucleus. A super-massive BH is surrounded by an accretion disc and a thicker torus. Relativistic jets can be formed parallel to the spinning axis. Figure taken from [28].

Gamma-ray bursts Gamma ray bursts (GRB) are assumed to be caused by massive star collapses or collisions of compact objects. They emit gamma-rays with energies of order of one solar mass over durations of seconds to minutes. Thus, GRB are one of the most luminous known astrophysical objects. After the actual burst, GRB emit an afterglow of less energetic photons. Via thermal neutrinos, shocked protons or decoupled neutrons, neutrinos of energies between MeV and GeV could be produced. [21]

Other extra-galactic sources Furthermore, extra-galactic neutrinos could be produced in starburst galaxies. Starburst galaxies are characterized by their outstandingly high rate of star formation [25]. Another possible concept are cosmogenic neutrinos. Their existence is implied by a cutoff in the ultra-high energy cosmic ray (UHCR) spectrum. Accordingly, at very high energies, the UHCR protons interacting with the cosmic microwave background could cause a flux of ultra-high energy neutrinos. [4]

Galactic sources Additionally, galactic neutrino sources are introduced. Neutrinos coming from galactic sources are assumed to be produced in the same way as extra-galactic neutrinos (cf. chapter 2.2.1). However, one important difference in the spectrum is the maximum neutrino energy. Given the maximum proton energy in galactic sources of $E_p < 3 \cdot 10^{18}$ eV, galactic neutrinos have a lower maximum energy than extragalactic neutrinos. This allows to distinguish between neutrinos from different sources. Also galactic neutrinos come mostly from the direction of the galactic plane. Among others, possible galactic neutrino emitters are supernova explosions, supernova remnants, microquasars, pulsars and pulsar wind nebulae. [4, 17]

2.2.3 Atmospheric neutrino background

The main background in cosmic neutrino detection are atmospheric muons and neutrinos. Those are produced in airshowers induced by primary CRs interacting in the upper atmosphere. In this hadron-hadron interaction (e.g. CR proton with atmospheric nucleon) secondary mesons, such as charged pions and kaons, and muons are produced. When the secondary mesons decay, they produce neutrinos. The dominant production channels are [24]:

$$\pi^\pm \rightarrow \mu^\pm + \nu_\mu(\bar{\nu}_\mu) \quad (2.11)$$

$$K^\pm \rightarrow \mu^\pm + \nu_\mu(\bar{\nu}_\mu) \quad (2.12)$$

$$K_L^0 \rightarrow \pi^\pm + e^\mp + \bar{\nu}_e(\nu_e) \quad (2.13)$$

The atmospheric neutrino spectrum can be described by an $\sim E^{-3.7}$ behavior while the primary spectrum follows an $\sim E^{-2.7}$ power law. The latter is about one order of magnitude flatter, because a considerable fraction of the secondary mesons interact before decaying. The neutrinos emerging in the described process are referred to as conventional atmospheric neutrinos, while prompt atmospheric neutrinos emerge from the decay of heavier charmed mesons. [4]; The spectra of atmospheric neutrinos and astrophysical neutrinos are visualized in figure 2.5.

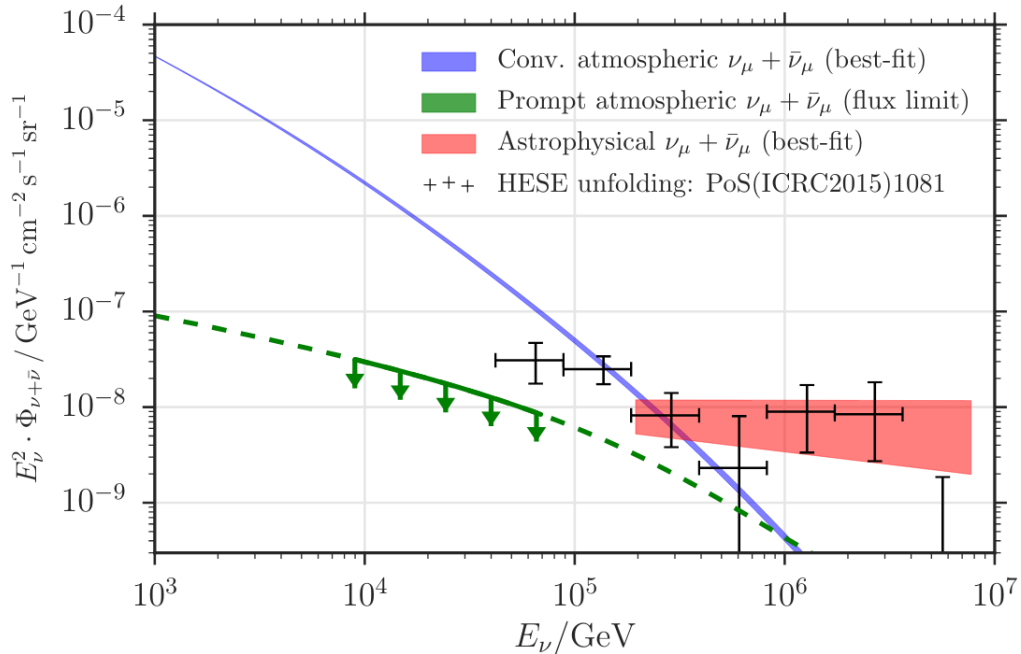


Figure 2.5: Neutrino spectra for atmospheric (blue and green) and astrophysical (black and red) neutrinos. Astrophysical neutrinos follow a harder spectrum than atmospheric neutrinos. Figure taken from [12].

3 Point-source search in IceCube

This chapter provides information on the IceCube detector and the point-source search for astrophysical neutrino sources. It covers a functional description of the detector and its instrumentation, as well as basic neutrino event reconstruction and selection methods and the analysis method used in the following point-source search.

3.1 The IceCube Neutrino Observatory

The IceCube neutrino observatory is a large volume neutrino detector, located near the Amundsen Scott South Pole Station at the geographic South Pole. It is embedded in the arctic ice, reaching depths of about 2500 meters. The detector consists of the main in-ice array that contains also a denser instrumented inner part called DeepCore and a surface cosmic ray air shower array, called IceTop. [1]; An illustration of the detector is shown in figure 3.1.

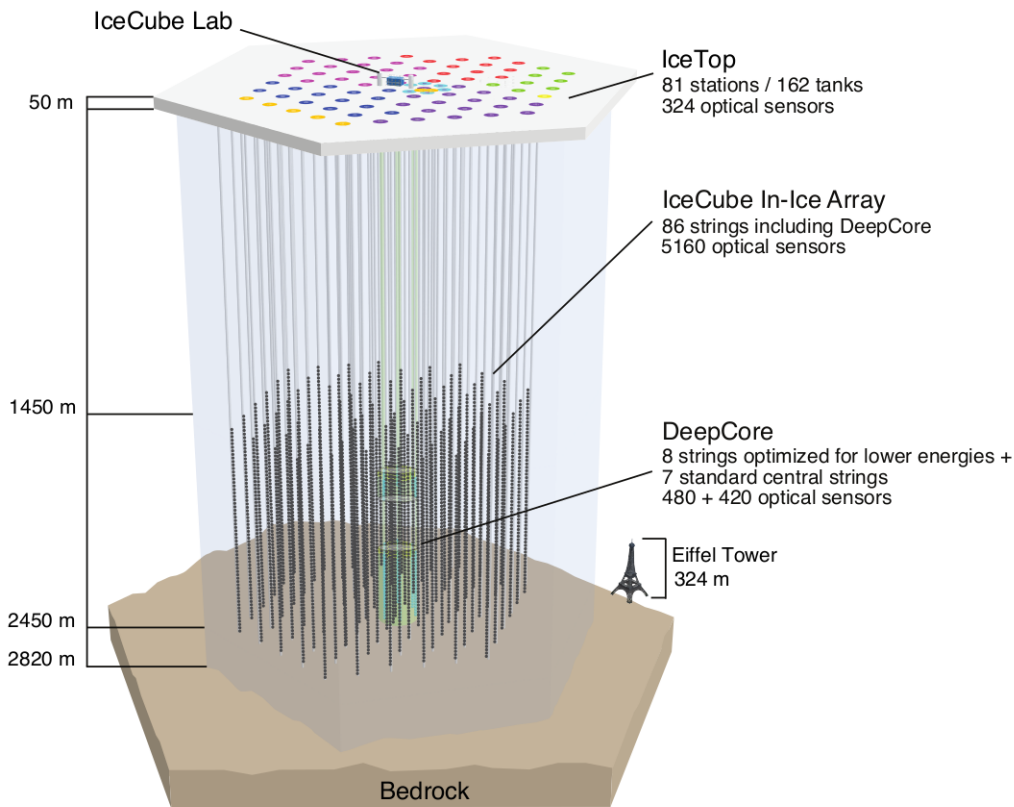


Figure 3.1: Illustration of the IceCube detector. It consists of the IceCube Lab (laboratory on the surface above the detector), the IceTop array (surface array to detect cosmic ray air showers) and the IceCube in-ice array (main part of the detector) with the DeepCore (denser instrumented inner part to detect neutrinos with lower energies down to 10 GeV). Figure taken from [10].

3.1.1 Functional description of the detector

The IceCube detector is a 1 km^3 hexagonal assembly of 5160 digital optical modules (DOMs) attached to 86 vertical strings in depths of 1450 to 2450 meters (cf. figure 3.1). The enormous detection volume is necessary because of the small cross section of neutrino interactions and the low expected neutrino flux from AMS on Earth. The DOMs are light sensor and data acquisition units. They are embedded in highly pressure resistant glass spheres and contain a downward-facing 25 cm diameter photo multiplier tube (PMT), an LED Flasher Board and other boards for data acquisition, control and calibration. Digitized, time-stamped PMT signals recorded in the DOMs are transmitted via wires to the IceCube Laboratory at the surface. The instrumentation is described in more detail in [10].

IceCube is designed to detect neutrinos with energies above $\sim 100 \text{ GeV}$. The neutrinos interacting inside or close to the detector volume scatter deeply inelastic with the nuclei in the ice molecules as explained in chapter 2.1.3. The so produced charged secondary particles travel through the ice faster than the speed of light in this medium. Due to constructive polarization effects, they then emit Cherenkov photons in a cone-like pattern. These can be detected in the DOMs. The primary neutrino's direction and energy can then be reconstructed considering the amount of photons and their arrival times (cf. chapter 3.2.2). A muon, emitting Cherenkov radiation, is illustrated in figure 3.2. The opening angle of the Cherenkov cone ϑ_C depends on the refractive index n of the medium ($n \simeq 1.32$ for ice) and the particle's velocity in units of the vacuum speed of light. Before their detection, photons can scatter or can be absorbed due to ice properties and impurities, which has to be taken into account in the reconstruction (cf. chapter 3.2.2). [10, 24]

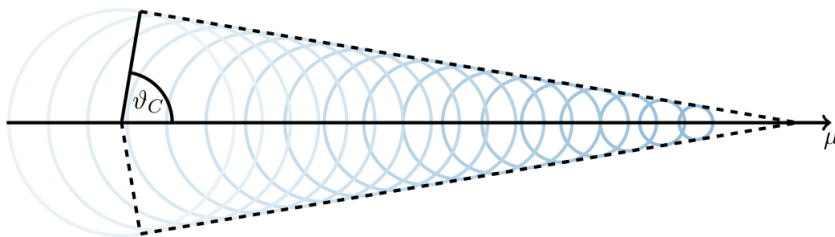


Figure 3.2: Illustration of a muon emitting cone-like Cherenkov radiation. The muon is traveling to the right. The opening angle ϑ_C of the Cherenkov cone depends on the refractive index of the medium and the particle's velocity. Figure taken from [24].

3.1.2 Data acquisition and filtering

A photon (or several photons) reaching a PMT and inducing a current is called a hit. A hit is defined by a time stamp and the waveform information collected for $\sim 6.4 \mu\text{s}$ [16]. A hit exceeding the threshold of 0.25 pe, with one pe corresponding to a single photoelectron, continues as a so called DOM launch. Due to the fact

that most DOM launches are caused by noise in the detector, spatial coincidences of launches are taken into account. Two local coincidences are distinguished: Hard local coincidences (HLC) signalize that at least two DOMs launch within $2\ \mu\text{s}$. Soft local coincidences (SLC) mean the launch of a single DOM. To assure that the tracks of the particles of interest are recorded, further triggering methods are applied. A commonly used trigger is the Simple Multiplicity 8 trigger which requires at least 8 HLC hits within $5\ \mu\text{s}$. All the information described above is then saved as an event. [16, 22]

To reduce the amount of data, different filters are applied. Events passing at least one filter are then stored offline. Relevant examples for filters are the Muon filter, the Cascade filter and a filter for extremely high-energy events (EHE) that requires a charge of at least 1000 pe. [24]

3.2 High-energy neutrino events

The higher the energy of the neutrino detected in IceCube, the higher the probability that the particle is coming from an astrophysical source [1]. Reaching higher energies, it is less probable to detect atmospheric neutrinos because of their softer spectrum (cf. figure 2.5). As soon as a neutrino that has a high probability to be of astrophysical origin gets detected, IceCube activates alerts for other telescopes [11]. Those can then observe the reconstructed incoming direction. In the last ~ 10 years since IceCube was put into operation in 2010 in full configuration, about 80 high-energy track-like neutrino events have been recorded. For those events the analysis presented in chapter 4 and 5 was done. The in IceCube detected events have to be reconstructed (cf. 3.2.2) and selected (cf. 3.2.3), in order to be used in a point-source analysis. Different event topologies are explained in the following.

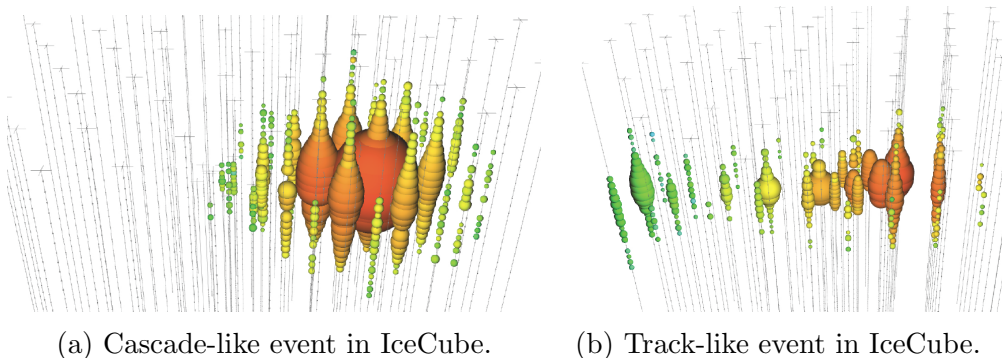


Figure 3.3: Two different types of IceCube events. Each PMT signal is illustrated by a sphere. The size correlates to the charge while the color shows the time course (from red to green). (a) Cascade-like events are particle showers near the interaction vertex. (b) Track-like events are caused by muons and have a typical range larger than the detector size. Figures taken from [2].

3.2.1 Event topologies

Depending on the underlying neutrino interaction, two main types of events can be distinguished. The important events in this work are muon induced track-like neutrino events because of their good angular resolution.

Cascade-like events Cascades are characterized by particle showers near the neutrino interaction vertex. They are produced in NC processes of neutrinos of all flavors and in electron neutrino CC processes (cf. chapter 2.1.3). The hadronic cascade at the neutrino vertex overlaps with an electromagnetic cascade induced by the outgoing electron. Because of the relatively short path lengths and the scattering of emitted photons, cascades appear spherically shaped in the detector. For cascade-like CC events the whole energy of the incoming neutrino can be deposited in the detector, for NC processes the outgoing lepton carries away a certain fraction. The origin direction of cascade causing neutrinos can be determined with a median angular resolution of 10-15°. Their median resolution on the deposited energy is about 10-15%. [8, 7, 24]; A cascade-like event in IceCube is visualized in figure 3.3a.

Track-like events Tracks are caused mainly by muons, either from air showers or from muon neutrino CC processes along with a hadronic shower. Muon tracks above ~ 1 TeV have a range of several kilometers, which is larger than the detector size. Because the track can extend throughout the whole detector, the median angular resolution for track-like events can be better than 1°. The energy reconstruction for tracks can only provide a lower limit on the neutrino energy. This is because a considerable fraction of the energy can be carried away from the detector by escaping particles and the vertex position can be unknown. Track-like events sub-categorize in starting tracks and through-going tracks. For starting tracks the interaction vertex lies inside and for through-going tracks outside the detector volume. [8]; A track-like event in IceCube is visualized in figure 3.3b.

3.2.2 Event reconstruction

Depending on the neutrino's direction and energy, astrophysical neutrinos can be discriminated from atmospheric background. Therefore, the direction and the energy of the detected neutrinos get reconstructed based on the properties of the recorded events (cf. chapter 3.1.2). Here the focus lies on the reconstruction of track-like muon events because they are the most interesting events for the point-source search in this work. Most reconstruction algorithms in IceCube are applied to the events successively. First, simple first-guess methods are applied, followed by more complicated and time-consuming, but more accurate techniques. [17, 22]

Directional reconstruction

Reconstructing the neutrino's direction means fitting a linear track based on the data recorded before (cf. chapter 3.1.2) as accurately as possible. A track is defined by a direction (θ, ϕ) and a vertex position $\vec{x} = (x, y, z)$.

Line fit In the line fit, the sum of the squares of the distances between the fitted track and the hits detected in the DOMs are minimized. In the course of fitting the track, the least-squares optimization problem is solved:

$$\min_{t_0, \vec{x}_0, \vec{v}_0} \sum_{i=1}^N \rho_i(t_0, \vec{x}_0, \vec{v}_0)^2, \quad (3.1)$$

where

$$\rho_i(t_0, \vec{x}_0, \vec{v}_0) = \|\vec{v}(t_i - t_0) + \vec{x}_0 - \vec{x}_i\|_2. \quad (3.2)$$

In this context \vec{x}_i and t_i are the position and the time of the i th of the N hits. The reconstructed track has a velocity \vec{v} and passes point \vec{x}_0 at time t_0 . The line fit is used as a seed to further more complicated reconstructions. [3]

Maximum likelihood reconstructions The further reconstructions take physical effects such as scattering and secondary cascades along the muon track into account. In the course of the reconstruction the estimation of the set of unknown parameters \vec{a} (e.g. track parameters) based on a set of measured values \vec{x} is done by maximizing the likelihood $\mathcal{L}(\vec{x}|\vec{a})$ for independent observables x_i of \vec{x} :

$$\mathcal{L}(\vec{x}|\vec{a}) = \prod_i p(x_i|\vec{a}). \quad (3.3)$$

Here $p(x_i|\vec{a})$ is the probability density function that refers to the observation of x_i for a certain \vec{a} . In a simplified case, \vec{a} is composed of the following parameters:

$$\vec{a} = (\vec{r}_0, t_0, \hat{p}, E_0). \quad (3.4)$$

At a certain time t_0 a muon with energy E_0 passes an arbitrary point on the track \vec{r}_0 following a direction \hat{p} . The parameters are also illustrated in figure 3.4. The muon track reconstruction is explained in detail in [15].

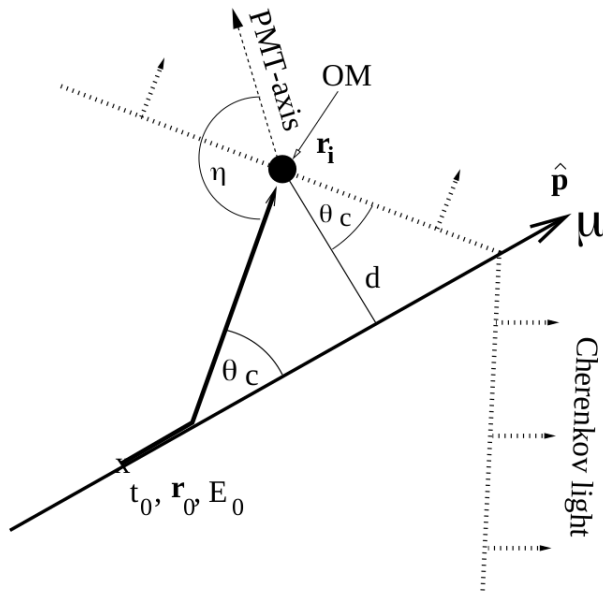


Figure 3.4: Parameters for track reconstruction using a maximum likelihood approach. The parameters refer to a Cherenkov light front generated by an infinitely long muon track. At time t_0 a muon with energy E_0 passes point \vec{r}_0 on the track in the direction \hat{p} . θ_C is the opening angle of the Cherenkov cone. The distance from the cone front to the reconstructed track is d . Figure taken from [15].

Energy reconstruction

The energy loss of muons is dominated by energy losses due to ionization and stochastic energy losses. The amount of Cherenkov light produced by the transiting secondary charged particles from neutrino interactions is proportional to the deposited energy. For CC electron and muon neutrino interactions the deposited energy is approximately the original neutrino energy. Thus the deposited energy in the detector can be used to calculate lower limits on the neutrino energy. The energy reconstruction in IceCube is also done by maximizing a likelihood function. The method is based on the assumption that the number of detected photons in a DOM follows a Poisson distribution with mean λ . The likelihood \mathcal{L} for an energy E eventuating in k detected photons is then for each DOM of the following type:

$$\mathcal{L} = \frac{\lambda^k}{k!} \cdot e^{-\lambda}. \quad (3.5)$$

The total likelihood function is then the product over the likelihoods of all involved DOMs. For point-source searches, the relevance of reconstructing the neutrino energy lies in being able to distinguish between astrophysical neutrinos and atmospheric background neutrinos, where the latter are expected to have lower energies. The energy reconstruction is explained in detail in [7].

3.2.3 Event selection

As a starting point for event selections for point-source searches, only events that already passed the muon filter (cf. chapter 3.1.2) are taken into account. In point-source searches one focuses on CC track-like muon events because of their better angular resolution. The majority of the detected neutrinos in IceCube are atmospheric background. The goal is to withdraw as many background events as possible and obtain a signal sample that contains only few background events while it should still contain as many signal events as possible. This is done in two steps: First obvious background and badly reconstructed events are removed by pre-cuts on the reconstructed variables. Then, a selection based on a boosted decision tree is applied. [22]

Preliminary data reduction IceCube events differ significantly depending on their incoming direction. For neutrinos from the northern hemisphere (zenith angle $\theta \geq 86^\circ$, up-going events) the Earth functions as a shield against atmospheric background, while neutrinos from the southern hemisphere (zenith angle $\theta \leq 85^\circ$, down-going events) can reach the detector volume independent of their energy. The neutrino absorption in Earth is illustrated in figure 3.5.

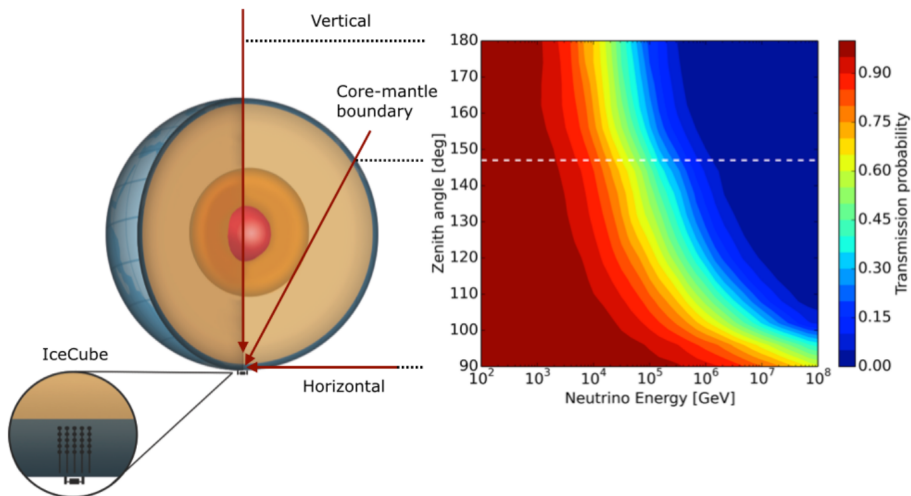


Figure 3.5: Illustration of neutrino absorption in Earth. Depending on the energy and the incoming angle the transmission probability varies. High transmission probability for low energies and horizontally incoming neutrinos (red) and low transmission probability for high energies and vertically incoming neutrinos that have to travel to larger parts of the Earth (blue). Figure taken from [13].

Cut-variables, depending on which the event sample gets reduced in the first step, are for example: The number of strings with at least one photon detecting DOM or the number of DOMs with a direct photon hit. A direct hit means a hit by a photon that reaches the DOM close to its expected arrival time, hence direct hits

are supposed to be less scattered. Another example is the reduced log likelihood of the track reconstruction fit. The actual cut-value of the cut-variable depends on the hemisphere the neutrino is coming from. [22]

Boosted decision tree selection In a second step a boosted decision tree algorithm is used to further reduce the background in the muon neutrino sample. When a decision tree algorithm is used, a Monte Carlo data set is divided into two subsets: A training sample and a test sample. By applying the decision tree to the training sample, the set gets divided into signal and background along several nodes referring to different criteria (e.g. PMT hits, energy). The test sample is then used to test the classifier after the training. A boosted decision tree uses increased weight for misclassified events which makes it less error-prone when a different sample than the training sample is used. The tested boosted decision tree algorithm can then be applied to the pre-selected muon neutrino sample. This reduces the amount of events in the sample by several orders of magnitude [22]. Boosted decision trees are explained in more detail in [27].

3.3 Point-source search method

The analysis done in this work uses especially the high-energy neutrino alert events from 10.5 years of IceCube data to search for astrophysical neutrino emission from their directions applying a time-independent analysis. The alerts are through-going and starting muon tracks with energies of $\gtrsim 100$ GeV [9]. An unbinned maximum likelihood formalism is used to find a local excess around the alert positions over the atmospheric background. Therefore the data from each investigated direction gets described by a background and a signal hypothesis: The null hypothesis \mathcal{H}_0 assumes that the set contains only background events. The signal hypothesis \mathcal{H}_S assumes that the set consists of background and signal events. The test statistic

$$\mathcal{TS} = -2 \log \left[\frac{\mathcal{P}(\text{Data}|\mathcal{H}_0)}{\mathcal{P}(\text{Data}|\mathcal{H}_S)} \right] \quad (3.6)$$

is the ratio of the probability of observing the used set under the assumption of the null hypothesis or of the signal hypothesis. Higher \mathcal{TS} values mean the signal-hypothesis is favored compared to lower \mathcal{TS} values. [22]

3.3.1 Unbinned likelihood ratio

The used likelihood function is the product over all events i of the superposition of the probability density (PDF) for signal \mathcal{S} and the PDF for background \mathcal{B} (cf. chapter 3.3.2):

$$\mathcal{L} = \prod_i \left[\frac{n_s}{N} \mathcal{S}_i(\vec{x}_i, \sigma_i, E_i; \vec{x}_s, \gamma) + \left(1 - \frac{n_s}{N}\right) \mathcal{B}_i(\delta_i, E_i) \right] \quad (3.7)$$

Here n_s is the number of expected signal events, N is the total number of signal and background events, \vec{x}_s is the source position and γ is the spectral index of the expected power law energy emission spectrum from the source. Referring to an event i , \vec{x}_i is the reconstructed source position, σ_i is the one sigma uncertainty of the directional reconstruction, E_i is the energy and δ_i is the declination of the reconstructed source position.

As described before, the \mathcal{TS} is the likelihood ratio of the null hypothesis ($n_s = 0$) over the best fit of the signal hypothesis ($n_s > 0$). Equation 3.6 can then be expressed as equation 3.8. This is later used to calculate a p-value which expresses the probability to be background (explained in more detail in chapter 4.3).

$$\mathcal{TS} = -2 \log \left[\frac{\mathcal{L}(n_s = 0)}{\mathcal{L}(n_s = \hat{n}_s)} \right] = 2 \sum_i \log \left[\frac{\hat{n}_s}{N_{obs}} \left(\frac{\mathcal{S}_i}{\mathcal{B}_i} - 1 \right) + 1 \right] \quad (3.8)$$

3.3.2 Signal and background PDFs

The signal and background PDFs both have a spatial and an energy component. The signal PDF can thus be expressed as

$$\mathcal{S}(\vec{x}_i, \sigma_i, E_i; \vec{x}_s, \gamma) = \mathcal{S}_{spatial} \cdot \mathcal{S}_{energy}. \quad (3.9)$$

For the spatial part it is assumed that signal events cluster around the source position \vec{x}_s , so that it is more likely for an event \vec{x}_i close to \vec{x}_s to be signal than for one more distant. The spatial signal PDF is then defined as a two dimensional Gaussian distribution around the source [22]:

$$\begin{aligned} \mathcal{S}_i(\vec{x}_i, \sigma_i, E_i; \vec{x}_s, \gamma) &= \mathcal{S}_i(\vec{x}_i, \sigma_i; \vec{x}_s) \cdot \mathcal{E}_S(E_i; \delta_i, \gamma) \\ &= \frac{1}{2\pi\sigma_i^2} \exp\left(-\frac{|\vec{x}_i - \vec{x}_s|^2}{2\sigma_i^2}\right) \cdot \mathcal{E}_S(E_i; \delta_i, \gamma) \end{aligned} \quad (3.10)$$

The energy factor \mathcal{E}_S is the PDF for a signal event with energy E_i , declination δ_i and spectral index γ .

The background PDF follows a similar structure ($\mathcal{B}(\vec{x}_i, E_i) = \mathcal{B}_{spatial} \cdot \mathcal{B}_{energy}$):

$$\begin{aligned} \mathcal{B}(\vec{x}_i, E_i) &= \mathcal{B}_i(\vec{x}_i) \cdot \mathcal{E}_B(E_i; \delta_i) \\ &= \frac{1}{2\pi} \cdot \mathcal{P}(\delta_i) \cdot \mathcal{E}_B(E_i; \delta_i) \end{aligned} \quad (3.11)$$

Because of the symmetry of the IceCube detector it can be assumed that the background is uniform over right ascension and varies spatially only depending on the declination. The energy distribution \mathcal{E}_B is from the same structure as explained for the energy PDF of signal events. [23]

4 Point-source search for neutrino excess from alert positions

The goal of this work is to set upper limits to the neutrino flux coming from possible astrophysical sources. The high-energy alert neutrinos that IceCube detected over the last decade are used as a source candidate catalog. The underlying concept is a time-independent point-source search. A skymap including all the investigated positions is shown in figure 4.1. The used sample contains the IceCube EHE events (extremely high-energy events), some of the IceCube HESE events (high-energy starting events, here referred to as AHES for alert high-energy starting) and up-going tracks with energies above 200 TeV from the IceCube diffuse sample (referred to as DIF events).

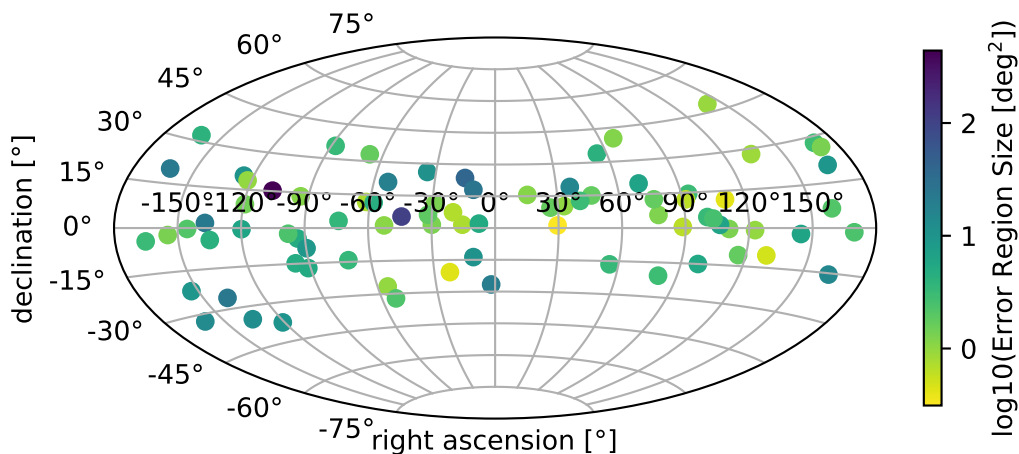


Figure 4.1: Skymap with observed high-energy alert event positions and error region sizes indicated by a colorbar on the right. Yellow markers indicate an error region of less than one square degree. Green markers indicate error regions between one and ten square degrees, while blue markers indicate error regions above ten square degrees. Right ascension and declination referring to ICRS (epoch = J2000). The clustering effect of the events around the horizon is due to the detector’s sensitivity in this area.

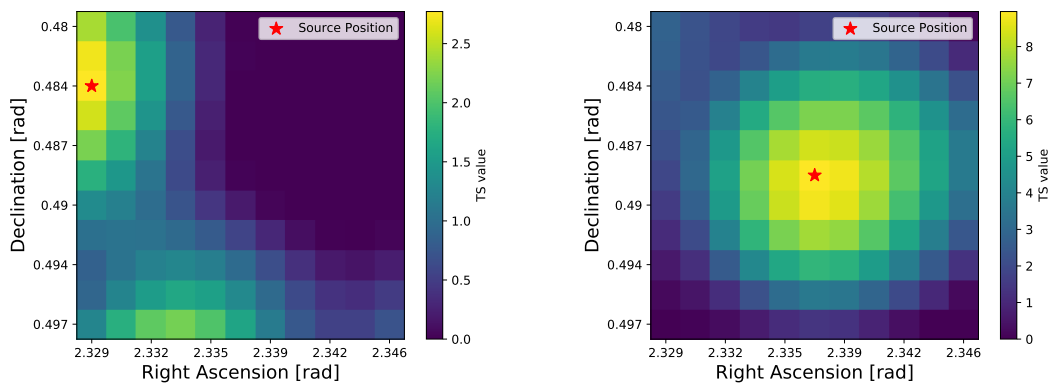
The information from chapter 2 and 3 is now used to follow the performed analysis in detail. In the first part of this chapter the provided data is explained as well as the used methods to prepare the data for the analysis. In the second part the concepts of p-value, sensitivity and discovery potential are discussed. The values for p-value, sensitivity and discovery potential presented here are a reproduction of a previous analysis, partially presented in [23].

4.1 Analysis approach

The alert data provided by IceCube contains the reconstructed right ascension (RA) and declination (DEC) of the alert position (including 50% and 90% angular uncertainties on RA and DEC), as well as the reconstructed energy. The time is also provided but not relevant in this analysis. The actual shape of the error regions was not accessible. Therefore, the shape of the error regions is approximated elliptic. In order to search for astrophysical emission from the alert positions, every position has to be fitted and trials have to be generated, as explained in the following.

4.1.1 Position fit

It is not sufficient to only take the reconstructed event coordinates, instead the source position has to be fitted for every alert direction based on the data from all ten years. For each of the investigated positions a rectangular grid with 0.1° spacing has been set. The grids are confined by the 90% confidence restrictions on RA and DEC. At each grid point the test statistic (cf. chapter 3.3.1) is maximized by fitting the number of signal events and the spectral index. The grid point with the highest \mathcal{TS} value is then considered as the source position. In figure 4.2 two plots for the \mathcal{TS} grids are shown, a background example on the left and a signal example with eight at the center injected events on the right.



(a) Map with only background fluctuations. (b) Map with eight injected signal events.

Figure 4.2: Maps of test statistic distributions of a possible neutrino source. The red star indicates the fitted source position. In (a) only background fluctuations are visible, while in (b) the pixel with the highest \mathcal{TS} value is the point where the signal events were injected.

The main analysis presented in the following uses an elliptic error region to imitate the original error region shape. The pixel with the highest \mathcal{TS} value is therefore not taken from the whole window, but from the ellipse defined by the restrictions on RA and DEC. In chapter 5.3 the results from the analysis with an elliptic error region are compared to the results of the same analysis using the rectangular error region.

4.1.2 Trial generation

For every investigated position 8000 background (BG) trials (zero injected signal events) and 1000 signal trials for one to 16 (sometimes 25) injected events respectively have been generated. This yields 16000 (sometimes 25000) signal trials for every position, which are then used with a Poisson weight considering the number of injected events. The emission is assumed to follow a power law spectrum with spectral index two. Every trial is a two dimensional array (also referred to as window) with the size of the considered error region divided into the 0.1° grid points. Every grid point (also referred to as pixel) contains the following information: Right ascension, declination, maximized \mathcal{TS} -value, fitted number of signal events, fitted spectral index and a seed used for the generation.

For the background trials IceCube’s symmetry is exploited. As described in chapter 3.3.1, it can be assumed that the background is uniform in right ascension. Therefore for every declination all events get scrambled in right ascension and are then treated as a background sample. This is done 8000 times for each window to obtain the background trials. The signal trials are obtained by injecting events (here from one to 16 and for some positions to 25) using Monte Carlo simulations. The astrophysical emission is assumed to follow a Poisson distribution which is realized by using the signal trials Poisson-like.

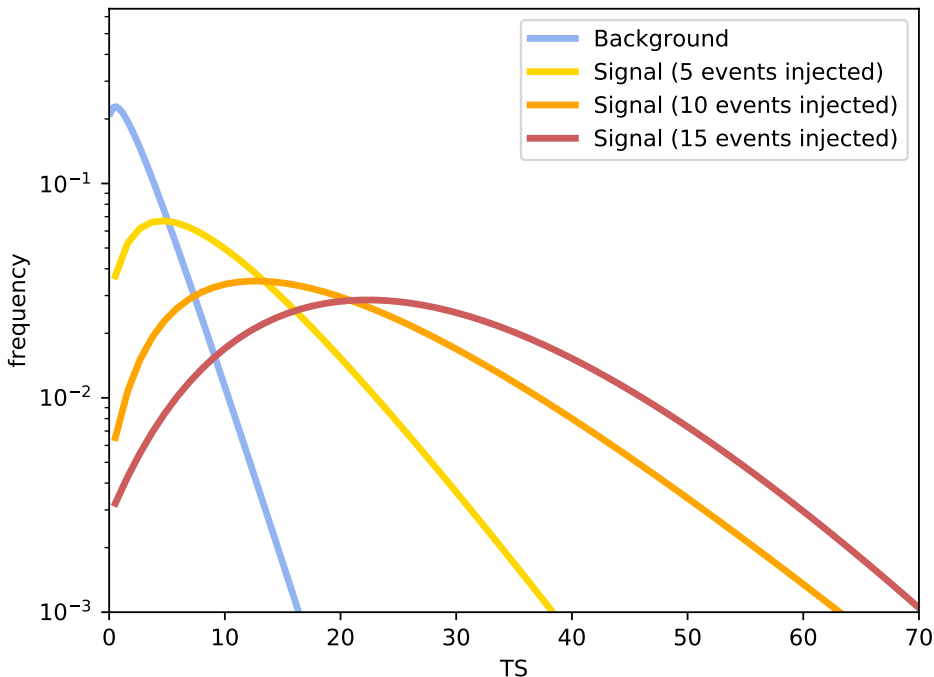


Figure 4.3: Background and signal distributions for a representative alert position. Shifted distribution towards higher \mathcal{TS} values for increasing number of injected events. The distributions are obtained applying a gamma distribution fit to the trial data.

In the next step for each window the pixel with the maximum \mathcal{TS} value of every trial is taken. This pixel corresponds to one fitted source position as described above. This way for every source there are 8000 background \mathcal{TS} values and 16 (and sometimes 25) times 1000 signal \mathcal{TS} values obtained. These distributions are shown in figure 4.3 for a representative source. The higher the number of injected events, the more the distribution gets shifted towards higher \mathcal{TS} values. Because of fluctuations not every background trial has the test statistic value zero. The larger the error region of a possible source, the higher is the effect of fluctuations which leads to a broadened background distribution.

4.1.3 Unit conversion

The results for sensitivity, discovery potential and flux limits are calculated in units of number of injected events. Every event that gets injected into a simulated signal trial stands for an astrophysical neutrino event detected in IceCube. The calculated number of injected events can then be converted into an energy flux emitted by the potential source. The necessary software is provided by IceCube. In the course of the conversion the source intensity is simulated using Monte Carlo data and the modeled detector response. The software considers the effective area of the detector and its sensitivity for events coming from the considered region in the sky. The effective area of the detector is the area an imaginary detector that measured every passing neutrino would have.

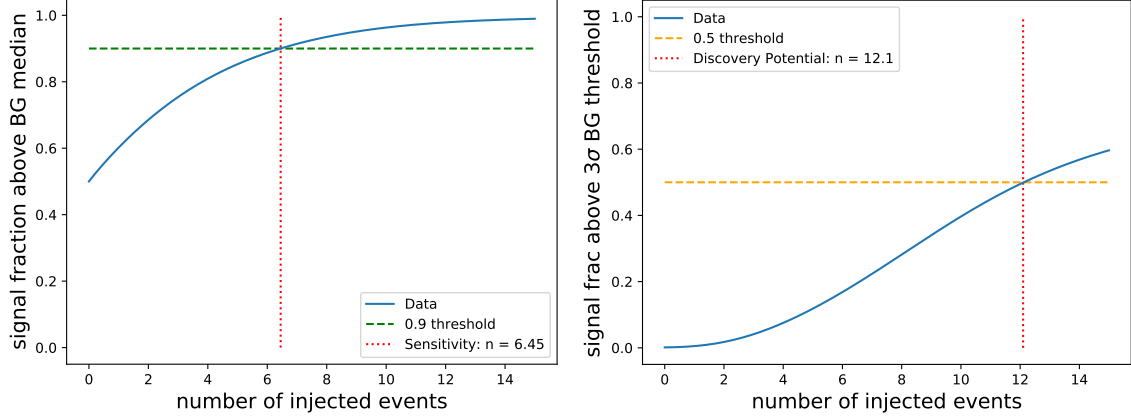
4.2 Sensitivity and discovery potential

Sensitivity and discovery potential provide information about the analysis' ability to distinguish signal from background in 90% of the cases and a threshold of when the observation is considered a discovery (here 3σ) in 50% of the cases respectively. Because of detector properties they depend beneath on the error region size only on the declination of the investigated position.

4.2.1 Analysis method

The methods to obtain sensitivity and discovery potential (and later the flux limits) follow a similar concept. First a certain cut-value is defined. This is e.g. the unblinded \mathcal{TS} value or the BG median. The background median is the 50% percentile of the BG \mathcal{TS} values. Afterwards, all signal trials for the observed position are combined in one sample. Each trial is weighted. The weight depends linearly on the trial length compared to the BG trials and Poisson-like on the number of injected events. This makes it possible to use the same trial sample for every tested number of injected events and only vary the weights. It also yields non-discrete and therefore more precise results. In the next step the number of injected events is evaluated for which the requirement of sensitivity, discovery potential or flux limit respectively

is fulfilled. The requirement is always of the kind: A certain fraction of the signal trials has to have a higher \mathcal{TS} value than the cut- \mathcal{TS} value. The calculated number of injected events can then be converted into an energy flux as described in 4.1.3. In figure 4.4 the analysis method is illustrated for an explanatory position for sensitivity (figure 4.4a) and discovery potential (figure 4.4b).



(a) Analysis method for sensitivity. (b) Analysis method for discovery potential.

Figure 4.4: (a) Analysis method for sensitivity. Depending on the number of injected events, a certain fraction of signal trials has a higher \mathcal{TS} value than the BG median. The first value for which the fraction is above 0.9 is the sensitivity (red dotted line). (b) Analysis method for discovery potential. Depending on the number of injected events, a certain fraction of signal trials has a higher \mathcal{TS} value than the 3σ BG threshold. The first value for which the fraction is above 0.5 is the 3σ discovery potential (red dotted line).

4.2.2 Sensitivity

The sensitivity is the threshold when astrophysical signal at the observed position can be distinguished from background with 90% confidence. It is thus defined by the number of injected events for which 90% of the signal trials have a higher \mathcal{TS} value than the background median. This is illustrated in figure 4.5a. The sensitivity can be expressed as

$$\text{Sensitivity} \Leftrightarrow n_{inj} \left[\frac{\# \text{ signal trials: } \mathcal{TS} > \text{BG Median}}{\# \text{ signal trials}} = 90\% \right]. \quad (4.1)$$

Because of the detector's symmetry the sensitivity depends on the declination of the observed position. Down-going signal events are mostly buried under the atmospheric background while up-going high-energy neutrinos are very likely to get absorbed when traveling through Earth (cf. figure 3.5). Therefore IceCube has the best sensitivity around the horizon. This effect is also visible in figure 4.1. The obtained sensitivities for all of the alert positions are presented in figure 4.6 and in table 1, 2 and 3.

4.2.3 Discovery potential

The discovery potential is the value starting from which the observation is seen as a discovery. In this work the values for 3σ discoveries are presented. Another common value would be the 5σ discovery potential. A 3σ discovery is defined by a 3σ confidence level. That means the remaining probability to having falsely declared background as signal is only 3σ . This corresponds to a probability of 0.135%. Here the discovery potential is thus calculated as the number of injected events for which only 3σ of the background trials have a higher \mathcal{TS} value than 50% of the signal trials. This is illustrated in figure 4.5b. The discovery potential can be expressed as

$$\text{Discovery Pot.} \Leftrightarrow n_{inj} \left[\frac{\# \text{ signal trials: } \mathcal{TS} > 3\sigma \text{ BG threshold}}{\# \text{ signal trials}} = 50\% \right]. \quad (4.2)$$

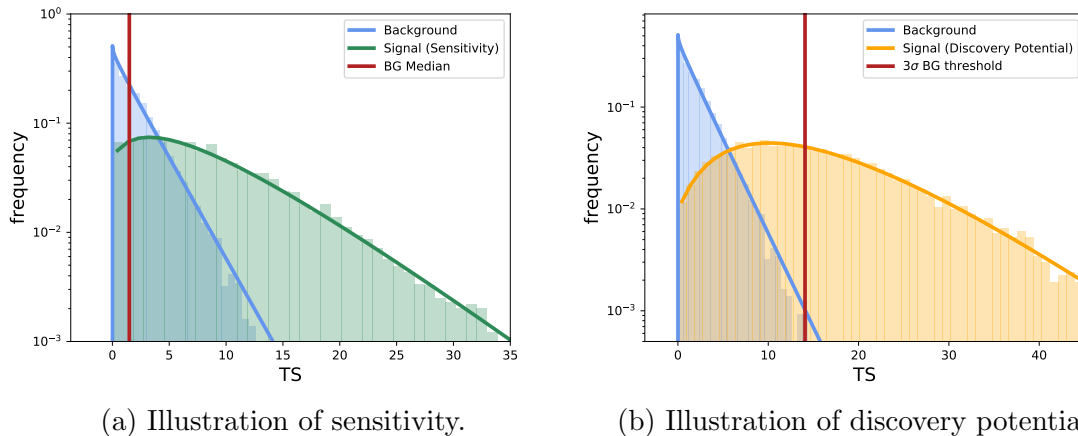


Figure 4.5: (a) The sensitivity for a direction is defined by the number of injected events for which 90% of the signal trials have a higher test statistic value than the BG median. This means signal can be distinguished from BG with 90% confidence. (b) The 3σ discovery is defined by the number of injected events for which only $3\sigma \cong 0.135\%$ of the BG trials have a higher test statistic value than 50% of the signal trials. This means BG is falsely declared as signal with a remaining probability of 0.135%.

The obtained discovery potentials for all of the alert positions are also presented in figure 4.6 and in table 1, 2 and 3. Figure 4.6 shows the results for sensitivity and discovery potential for the investigated positions. Both follow the same course: At the horizon the detector is most sensitive, which means it is already sensitive to lower energy fluxes. For down-going events the sensitivity gets worse relatively fast depending on the angle because of the increasing atmospheric background. For up-going events the sensitivity gets worse the further the neutrinos have to travel through Earth, because of the increasing absorption probability. The latter effect is low compared to the decreasing sensitivity due to atmospheric background. Also a

dependency on the error region size is visible, indicated by whitened out dots for increasing error regions.

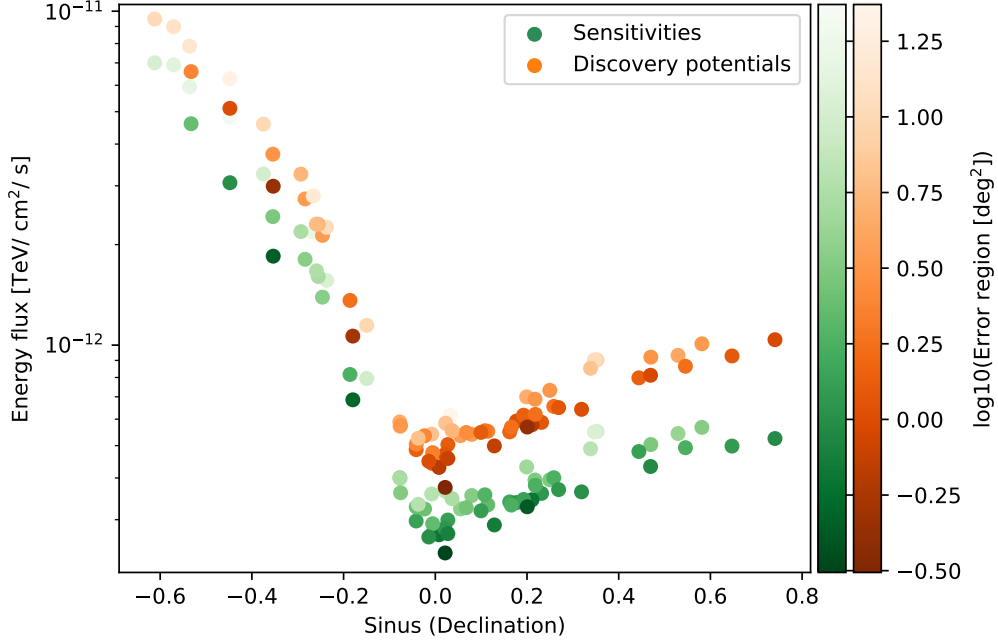


Figure 4.6: Sensitivity (green) and 3σ discovery potential (orange) for alert positions. Visible dependency on declination: IceCube is most sensitive at the horizon, decreasing sensitivity for down-going events due to huge atmospheric background and for up-going events due to absorption in Earth. Dependency on error region size indicated by whitened out dots for larger error regions.

4.3 P-values

The p-value expresses the probability for the source to only be background. Hence, high p-values mean that the analysis favors the null hypothesis while low p-values mean that the signal hypothesis is favored. For the explanation of the considered hypotheses cf. chapter 3.3.1. The p-value is defined as the fraction of background trials that have a higher \mathcal{TS} value than the observed unblinded \mathcal{TS} value of the position. The p-value can be expressed as equation 4.3. In figure 4.7 the calculation of the p-value is illustrated for the alert position of DIF32 as an example. In this work all p-values have been calculated without trial correction.

$$\text{p-value} = \frac{\# \text{ BG-Trials: } \mathcal{TS}_{\text{BG}} > \mathcal{TS}_{\text{obs}}}{\# \text{ BG-Trials}} \quad (4.3)$$

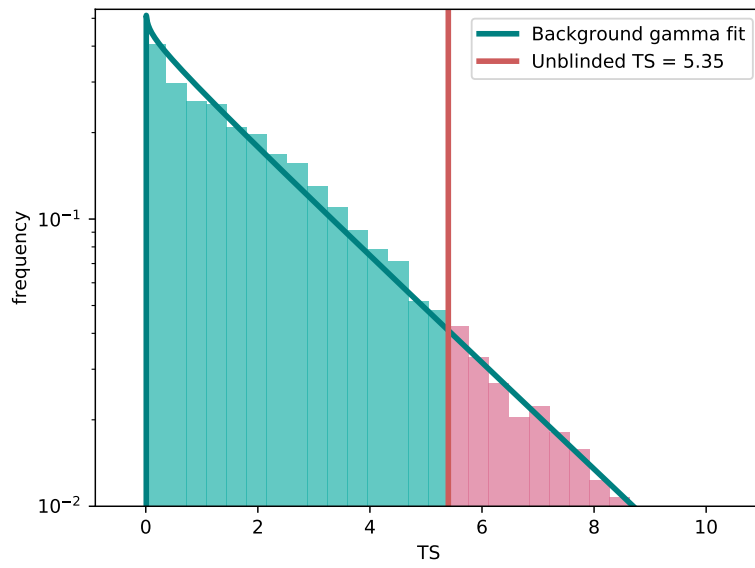


Figure 4.7: Explanatory illustration of p-value calculation for position of DIF32. The p-value is the fraction of BG trials with a \mathcal{TS} value higher than the unblinded \mathcal{TS} value. In this exemplary case the fraction and hence the p-value is 0.086 (cf. table 3).

5 Upper limits on astrophysical neutrino emission

This chapter covers the determination of upper flux limits for the investigated alert positions. For every position the analysis was first performed individually, followed by the analysis of the stacked positions. In the end two comparison studies are presented.

The upper flux limit $\Phi_{90\%}$ stands for the maximum energy flux that a possible point-source could emit and still be excluded with the current methods with 90% confidence. It is therefore assumed that the position would have been excluded as a source with a probability of less than 10% if it emitted a higher flux than $\Phi_{90\%}$. For this analysis this means that the flux limit for every source is given by the number of injected events for which 90% of the signal trials have a higher test statistic value than the observed test statistic value. If the observed \mathcal{TS} value is lower than the background median, the upper flux limit equals the sensitivity. The flux limit can be expressed as

$$\Phi_{90\%} \Leftrightarrow n_{inj} \left[\frac{\# \text{ signal trials: } \mathcal{TS} > \mathcal{TS}_{obs}}{\# \text{ signal trials}} = 90\% \right]. \quad (5.1)$$

The analysis method is the one explained in chapter 4.2.1. In figure 5.1 the upper flux limit is illustrated for an explanatory position.

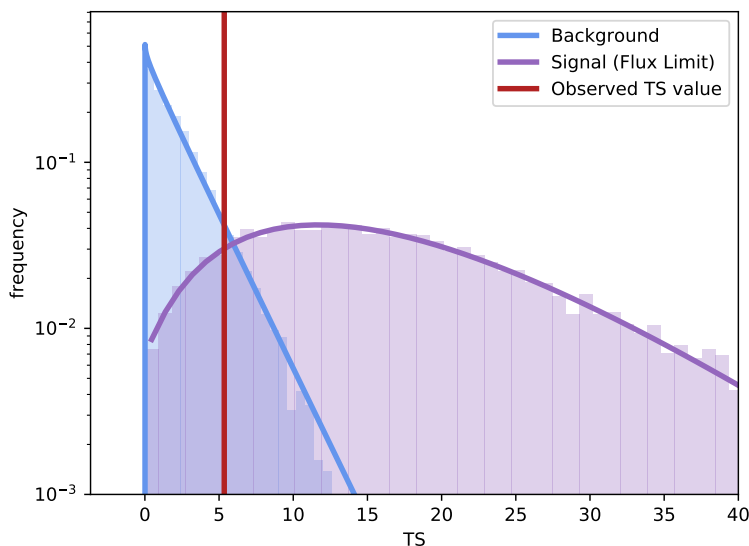


Figure 5.1: Illustration of upper flux limit with 90% confidence. The upper flux limit sets the emission threshold above which a source would not have been excluded with 90% confidence. In this analysis it is the number of injected events for which 90% of the signal trials have a higher \mathcal{TS} value than the unblinded \mathcal{TS} value.

5.1 Individual analysis

The upper flux limit was calculated for every investigated position individually as explained above. The results are presented in table 1, 2 and 3. The most interesting flux limits are the ones that are higher than the sensitivity ($\mathcal{TS}_{\text{obs}} > \text{BG Median}$). For those, a range is given in which a possible astrophysical emission could still lie without being excluded with the current setup. This is especially relevant for the sources whose discovery potential lies between sensitivity and upper flux limit ($\text{sens} < dp < \Phi_{90\%}$). The respective positions are highlighted **bold** in table 1, 2 and 3. For the positions that fulfill the condition $\text{sens} < dp < \Phi_{90\%}$ also the p-value is low compared to the remaining ones (between 0.022 and 0.168). This makes the respective source candidate positions the most significant ones of the investigated sample.

In figure 5.2 the results for all positions are shown. The colorbar on the right indicates the error region size as seen before. The same trend towards higher fluxes for up- and down-going events as for sensitivity and discovery potential (cf. figure 4.6) is visible. The most significant positions for which also the condition $\text{sens} < dp < \Phi_{90\%}$ is fulfilled are marked with a red circle. It is visible that for those positions the flux limit is relatively high compared to other potential sources with similar declination.

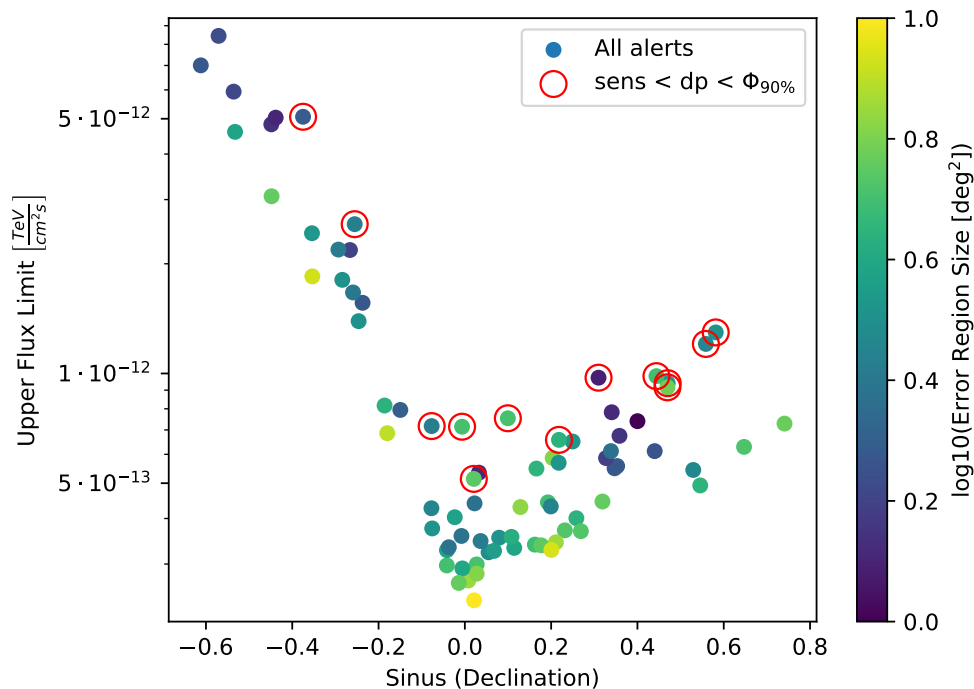


Figure 5.2: Correlation of $\Phi_{90\%}$ with declination and error region. Error region size indicated by colorbar on the right. The positions marked with a red circle have the most significant p-values and fulfill the condition $\text{sens} < dp < \Phi_{90\%}$. For down-going events ($\sin(\delta) < 0$) the flux limits increase due to atmospheric background. For up-going events ($\sin(\delta) > 0$) they increase due to absorption in Earth.

Results of the individual analysis

In this section the results of the individual analysis are presented. In the skymap in figure 5.3 the most significant positions that also fulfill the condition $sens < dp < \Phi_{90\%}$ are marked with a red star.

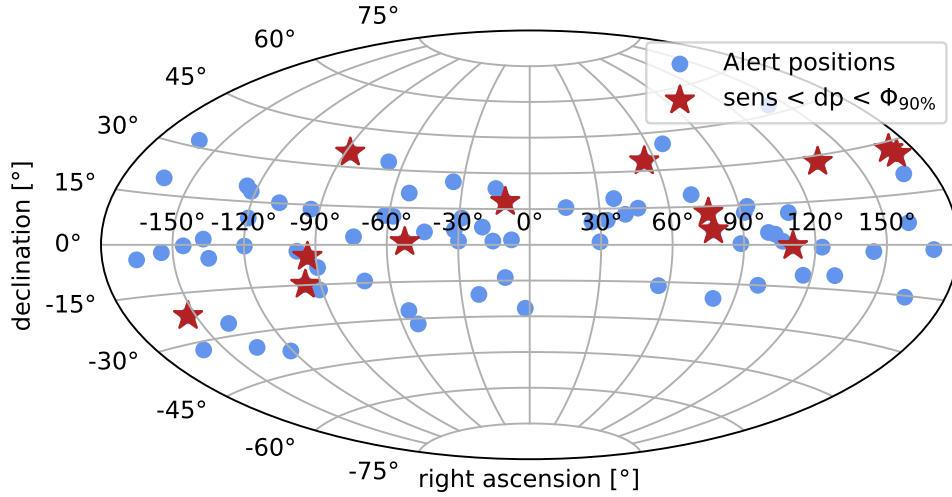


Figure 5.3: Skymap with alert positions. The most significant ones are marked as red stars. These also fulfill the condition $sens < dp < \Phi_{90\%}$.

Table 1, 2 and 3 show for every investigated position the following values: Right ascension, declination, \mathcal{TS} value, p-value, sensitivity, discovery potential and the upper flux limit $\Phi_{90\%}$. The most significant positions that also fulfill the condition $sens < dp < \Phi_{90\%}$ are highlighted **bold**.

Results AHES events							
Name	ra [°]	dec [°]	TS	p-value	sens [1]	dp [1]	$\Phi_{90\%}$ [1]
AHES2	111.36	-0.37	9.836	0.022	2.723	4.421	7.144
AHES4	67.26	40.32	2.49	0.369	4.985	9.28	6.289
AHES7	166.64	21.72	4.798	0.491	5.51	9.028	5.573
AHES9	207.17	-21.03	9.535	0.152	32.545	45.897	50.625
AHES11	239.82	-38.85	3.764	0.89	70.057	94.725	70.057
AHES12	55.12	-17.08	3.42	0.73	18.068	27.4	18.068
AHES13	159.1	6.38	2.488	0.562	3.322	5.52	3.322
AHES14	80.46	-20.75	2.827	0.7	24.257	37.298	24.257
AHES15	239.41	0.23	5.03	0.513	3.582	5.411	3.582
AHES17	240.77	9.24	0.105	0.941	3.392	5.498	3.392
AHES18	200.3	-33.61	6.023	0.663	59.34	78.562	59.34
AHES19	41.73	12.19	4.739	0.264	3.944	6.888	5.688
AHES20	304.95	-26.19	2.294	0.586	30.64	51.178	30.64
AHES21	224.47	-25.14	7.626	0.641	50.345	63.836	50.345
AHES22	162.36	-14.12	5.19	0.877	21.815	27.968	21.815
AHES23	144.0	-1.68	3.262	0.836	3.336	5.262	3.336
AHES24	225.97	-34.22	7.807	0.338	69.053	89.814	84.398
AHES25	356.54	-27.61	5.582	0.876	48.269	62.783	48.269
AHES26	307.74	-32.79	3.439	0.546	46.02	65.921	46.02
AHES27	269.71	-17.21	4.278	0.79	21.877	32.508	21.877
AHES28	337.42	-20.99	0.352	0.759	18.466	29.91	18.466

Table 1: Results for AHES (alert high energy starting) events. Sensitivity, discovery potential and upper flux limit $\Phi_{90\%}$ in units [1] = $\cdot 10^{-13} \left[\frac{\text{TeV}}{\text{cm}^2 \text{s}} \right]$. The most significant positions that also fulfill the condition $sens < dp < \Phi_{90\%}$ are highlighted **bold**.

Results EHE events							
Name	ra [°]	dec [°]	TS	p-value	sens [1]	dp [1]	$\Phi_{90\%}$ [1]
EHE1	330.46	10.91	2.791	0.356	3.449	6.168	4.43
EHE2	88.13	0.46	0.217	0.848	2.704	4.301	2.704
EHE3	307.71	1.45	5.997	0.113	2.824	4.699	5.137
EHE4	116.64	-10.81	0.806	0.824	8.167	13.611	8.167
EHE5	267.38	-5.17	6.929	0.1	3.989	5.709	7.172
EHE6	238.11	18.78	2.525	0.386	3.635	6.422	4.453
EHE7	171.74	26.26	6.827	0.055	4.801	7.582	9.833
EHE8	70.44	19.89	4.978	0.36	4.892	8.523	6.123
EHE9	205.52	-1.96	2.371	0.595	2.973	4.863	2.973
EHE10	129.81	-10.67	0.0	0.836	6.857	10.641	6.857
EHE11	301.45	10.5	2.887	0.66	4.317	6.998	4.317
EHE12	289.07	-14.25	3.831	0.581	13.918	21.307	13.918
EHE13	344.63	1.83	1.865	0.479	2.726	4.575	2.823
EHE14	292.85	32.6	0.093	0.943	4.929	8.643	4.929
EHE15	349.54	-13.05	4.81	0.714	15.629	22.539	15.629
EHE16	110.87	11.49	0.01	0.875	3.28	5.683	3.28
EHE17	169.9	-0.88	4.937	0.342	3.231	5.351	4.032
EHE18	328.19	6.65	0.012	0.988	3.562	5.539	3.562
EHE19	54.85	33.76	8.67	0.055	5.827	9.518	12.052
EHE20	103.47	4.18	2.308	0.658	3.26	5.475	3.26
EHE21	193.48	-4.43	2.741	0.476	3.612	5.744	3.757
EHE22	261.99	-2.29	1.704	0.86	3.275	5.051	3.275
EHE23	264.08	-15.25	8.024	0.168	16.053	23.009	25.685
EHE24	352.63	2.98	1.958	0.889	3.469	5.546	3.469
EHE25	214.03	-0.89	0.17	0.98	2.919	4.765	2.919
EHE26	122.61	-0.39	2.003	0.538	2.662	4.488	2.662
EHE27	45.68	14.82	1.73	0.667	4.007	6.552	4.007
EHE28	99.0	-15.02	1.38	0.987	16.685	23.033	16.685
EHE29	77.15	5.52	8.276	0.04	3.189	5.478	7.536
EHE30	339.9	7.49	2.899	0.264	2.893	4.991	4.3
EHE31	269.4	-9.71	3.991	0.694	7.942	11.462	7.942

Table 2: Results for EHE (extremely high energy) events. Sensitivity, discovery potential and upper flux limit $\Phi_{90\%}$ in units [1] = $\cdot 10^{-13} [\frac{TeV}{cm^2 s}]$. The most significant positions that also fulfill the condition $sens < dp < \Phi_{90\%}$ are highlighted **bold**.

Results DIF events							
Name	ra [°]	dec [°]	TS	p-value	sens [1]	dp [1]	$\Phi_{90\%}$ [1]
DIF1	29.32	1.32	0.198	0.735	2.385	3.748	2.385
DIF2	297.92	11.98	4.161	0.156	3.399	5.977	5.864
DIF3	343.86	23.19	4.276	0.966	7.398	—	7.398
DIF4	141.25	47.32	2.389	0.312	5.251	10.38	7.286
DIF5	306.96	19.44	6.331	0.454	6.276	—	6.744
DIF7	266.87	13.4	1.833	0.482	3.597	5.87	3.712
DIF10	284.75	3.32	2.097	0.769	3.232	5.353	3.232
DIF12	236.9	19.35	4.352	0.612	5.494	9.033	5.494
DIF13	273.23	35.94	9.543	0.031	5.671	9.132	12.962
DIF15	216.82	1.18	7.963	0.419	4.685	6.173	5.343
DIF16	36.05	19.68	4.762	0.669	5.859	—	5.859
DIF17	199.63	32.59	1.474	0.838	5.435	9.317	5.435
DIF18	329.37	1.75	1.534	0.666	2.993	5.038	2.993
DIF20	170.24	27.95	5.817	0.14	5.038	9.203	9.404
DIF21	93.75	13.99	5.736	0.185	3.95	7.32	6.506
DIF22	225.28	-3.88	3.482	0.46	4.01	5.887	4.268
DIF23	32.41	10.0	0.256	0.873	3.376	5.922	3.376
DIF25	349.6	17.1	10.205	0.157	6.341	8.415	9.737
DIF26	105.56	1.66	5.866	0.378	3.648	5.836	4.401
DIF28	99.59	5.14	3.115	0.596	3.544	5.404	3.544
DIF29	91.76	12.18	1.293	0.509	3.442	5.775	3.442
DIF30	326.61	27.38	3.331	0.803	6.123	—	6.123
DIF32	133.81	27.72	5.349	0.086	4.33	8.123	9.163
DIF33	197.6	17.69	7.742	0.324	5.978	—	7.827
DIF36	26.38	10.21	4.612	0.202	3.318	5.676	5.484
DIF34	75.74	12.95	5.271	0.154	3.802	6.203	6.574
DIF35	15.21	15.69	1.785	0.552	3.692	6.498	3.692

Table 3: Results for DIF events (from diffuse sample). Sensitivity, discovery potential and upper flux limit $\Phi_{90\%}$ in units [1] = $\cdot 10^{-13} \left[\frac{\text{TeV}}{\text{cm}^2 \text{s}} \right]$. The most significant positions that also fulfill the condition $sens < dp < \Phi_{90\%}$ are highlighted **bold**.

5.2 Stacked analysis

The individual analysis (cf. 5.1) tests for every position if a neutrino excess over background is measurable from this direction. In the stacked analysis all possible sources are treated as a population of relatively low emitting sources and not seen as individual candidates. This way it is tested if from all possible sources in total an emission excess over background is measurable. This leads to the combination of all possible sources to one source-type candidate for which the analysis as described for the individual candidates is performed. Two different stacking methods are done and compared in the end: \mathcal{TS} value stacking and p-value stacking. For both analyses new stacked trials have to be generated. As for the individual analysis 8000 background trials and 1000 signal trials for every number of injected events are generated. The trials obtained as described in 4.1.2 are used as a starting point. The exact trial generation depends on the stacking method and is explained in the respective section in the following.

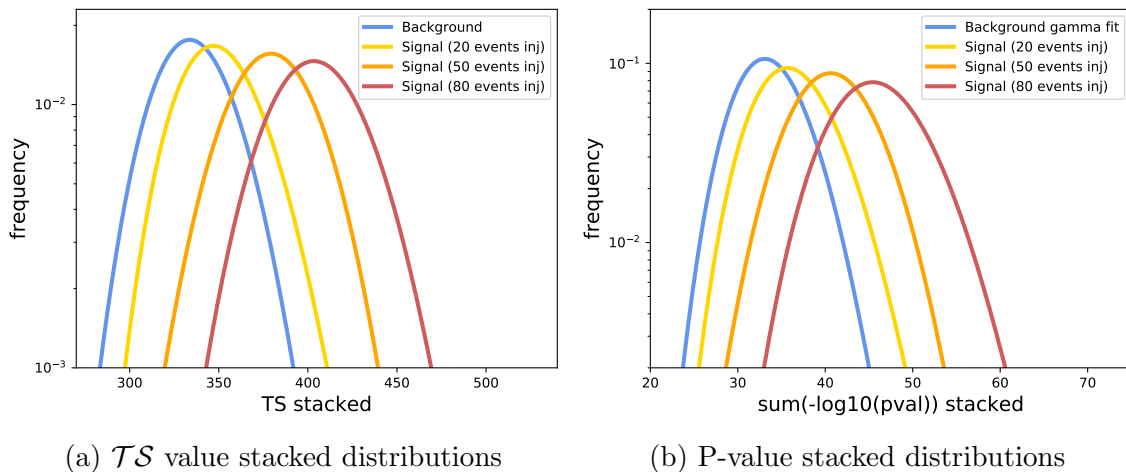


Figure 5.4: Distributions of the stacked analyses. All fitted with a gamma distribution. (a) Distributions of the \mathcal{TS} -value stacking. The \mathcal{TS} value of the stacked source is the sum of the single position's \mathcal{TS} values. Shifted distributions towards higher \mathcal{TS} values for increasing number of injected events. (b) Distributions of the p-value stacking. The $-\log_{10}p$ -value of the stacked source is the sum of the single position's $-\log_{10}p$ -values. Shifted distributions towards higher $-\log_{10}p$ -values for increasing number of injected events.

5.2.1 \mathcal{TS} value stacking

For the \mathcal{TS} value stacking the test statistic values of all possible sources are added to the stacked \mathcal{TS} value. Then the whole analysis is performed as seen before.

$$\mathcal{TS}_{\text{stacked}} = \sum_{i=1}^{\#\text{sources}} \mathcal{TS}_i \quad (5.2)$$

The \mathcal{TS} -stacked background trial is obtained by adding a background \mathcal{TS} -value of every position. The n -th trial entry of the stacked BG trial is therefore the sum of the n -th BG trial entries of all positions.

Then 1000 signal trials for every number of injected events starting from one have to be generated. For a signal trial with x injected events x single positions are randomly selected as signal. Multiple selections of single sources are allowed. Therefore every selected source has the additional information y how often it is selected. Higher y corresponds to a higher signal from the source. The not-selected positions are considered as background. One entry of the stacked signal trial with x injected events then consists of two added components: The sum of a random background trial entry of all positions that have not been selected as signal. Added to the sum of a random trial entry with y injected events of all the positions selected as signal. The latter component equals the event injection. This is repeated 1000 times for each $x \in [1, \text{maximum number of injected events}]$ to obtain 1000 signal trials for every number of injected events.

This way a distribution as shown in figure 5.4a is obtained. This distribution is the equivalent to figure 4.3 for the individual analysis. For the injection the signal trials are also weighted following a Poisson distribution. The distributions are shifted towards higher \mathcal{TS} values for higher numbers of injected events.

Using the obtained distributions one can calculate sensitivity, discovery potential, upper flux limit and p-value as for the individual analysis. Those are presented in chapter 5.2.3. The stacked equivalent to the unblinded \mathcal{TS} value is the sum of all unblinded \mathcal{TS} values. In figure 5.5 a background gamma fit for the \mathcal{TS} value stacking and the stacked \mathcal{TS} value as well as the BG median are shown. The stacked \mathcal{TS} value is 315.0. The stacked BG median is 335.03.

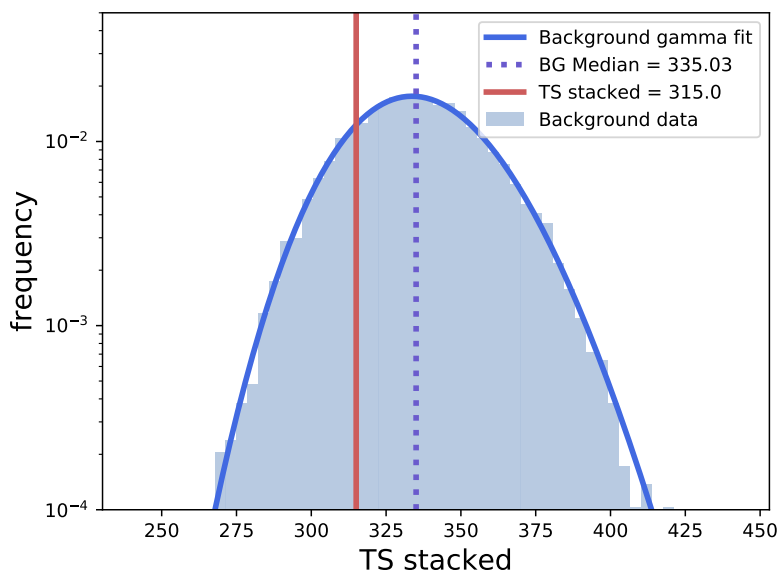


Figure 5.5: Stacked \mathcal{TS} value (315.0) compared to stacked BG median (335.03) and BG distribution including a gamma distribution fit.

The problem of the \mathcal{TS} value stacking is that the \mathcal{TS} values do not necessarily have the same meaning for every source. Depending on the background distribution source candidate positions with the same \mathcal{TS} value can result in different p-values. Therefor another stacking approach has been done as described in the following.

5.2.2 P-value stacking

To avoid the problem that the \mathcal{TS} value does not necessarily have the same meaning for every source candidate position (especially because of different background distributions due to different error regions) also a p-value stacking has been done. Instead of the sum of the \mathcal{TS} values the product of the local p-values is used. The total score is obtained by summing over the logarithms of the individual values. The negative value is taken to obtain a positive p_{stacked} and thus to be able to compare the results using the methods of the individual analysis.

$$p_{\text{stacked}} = \sum_{i=1}^{\#sources} -\log_{10} p_i \quad (5.3)$$

The trial generation in the p-value stacking is different from the \mathcal{TS} value stacking. The background distribution is obtained by taking an element of the background distribution (\mathcal{TS}_i^*) of a possible source position i and declaring it as the unblinded \mathcal{TS} value. Then a corresponding local p-value is calculated with the chosen value and the rest of the distribution $p(\mathcal{TS}_{\text{BG},i})$ as in equation 5.4. The distribution $p(\mathcal{TS}_{\text{BG},i})$ is fitted with a gamma distribution.

$$p_i = 1 - \int_0^{\mathcal{TS}_i^*} p(\mathcal{TS}_{\text{BG},i}) d\mathcal{TS} \quad (5.4)$$

Equation 5.4 equals equation 4.3 for an infinite distribution. The local BG p-value is calculated for every considered source position as in equation 5.4. Then a total score is calculated as in equation 5.3. This is repeated 8000 times to obtain the stacked BG trial. For the n -th entry of the stacked BG trial the n -th entry of the BG trial of source i is considered as \mathcal{TS}_i^* .

For a signal trial with x injected events x source positions are randomly selected similar to the \mathcal{TS} value stacking. Also here multiple selections are allowed and y stands for the number of selections. For every selected source a random \mathcal{TS} value from the signal trial with y injected events is taken and declared as \mathcal{TS}_i^* . The local p-value of the signal sources is calculated with equation 5.4 using also the BG distribution. The difference is that now \mathcal{TS}_i^* is from the signal trial instead of the BG trial. The local p-values of the not-selected positions, seen as background, are instead calculated by taking \mathcal{TS}_i^* from the background sample of the respective position. An entry in the stacked signal trial is then the logarithmic sum over the BG p-values of the not-selected positions added to the logarithmic sum over the signal p-values of the selected sources. The sums are always calculated as in equation 5.3. This

is also repeated 1000 times for each $x \in [1, \text{maximum number of injected events}]$ to obtain 1000 signal trials for every number of injected events as seen for the \mathcal{TS} value stacking.

This way a distribution as shown in figure 5.4b is obtained. This distribution is the equivalent to figure 4.3 for the individual analysis and to figure 5.4a for the \mathcal{TS} value stacking. For the injection the signal trials are again weighted following a Poisson distribution. The distributions are shifted towards higher scores for higher numbers of injected events.

Here again sensitivity, discovery potential, upper flux limit and p-value can be calculated using the obtained distributions as for the individual analysis. Those are also presented in chapter 5.2.3. The p-value stacked equivalent to the unblinded \mathcal{TS} value is the sum of the $-\log_{10}p$ -values of all investigated positions. In figure 5.5 a background gamma fit for the p-value stacking and the stacked $-\log_{10}p$ -value as well as the BG median are shown. The stacked $-\log_{10}p$ -value is 24.09. The stacked BG median is 33.41.

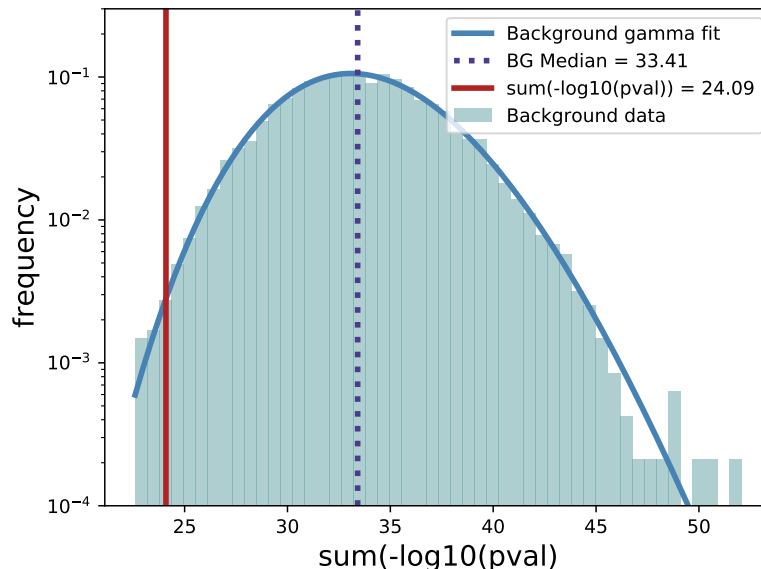


Figure 5.6: Stacked $-\log_{10}p$ -value (24.09) compared to stacked BG median (33.41) and BG distribution including a gamma distribution fit.

5.2.3 Stacking results and comparison

In table 4 the results for the \mathcal{TS} value stacking and the p-value stacking are presented in units of number of injected events and energy flux $\left[\frac{\text{TeV}}{\text{cm}^2\text{s}}\right]$. In both analyses the sensitivity, the 3σ discovery potential, the flux limit $\Phi_{90\%}$ and a p-value have been calculated. The p-value stacking is slightly more sensitive than the \mathcal{TS} value stacking. The \mathcal{TS} value stacking leads to a final p-value of 0.8171 and the p-value stacking of 0.8261. Hence no astrophysical neutrino excess over background is measurable with either of the described methods.

	\mathcal{TS} value stacking	$-\log_{10}p$ -value stacking
Sensitivity	$n_s = 38.95 \left(\hat{=} 6.74 \cdot 10^{-12} \frac{\text{TeV}}{\text{cm}^2\text{s}}\right)$	$n_s = 37.6 \left(\hat{=} 6.54 \cdot 10^{-12} \frac{\text{TeV}}{\text{cm}^2\text{s}}\right)$
Disc. pot. 3σ	$n_s = 86.25 \left(\hat{=} 14.98 \cdot 10^{-12} \frac{\text{TeV}}{\text{cm}^2\text{s}}\right)$	$n_s = 83.1 \left(\hat{=} 14.54 \cdot 10^{-12} \frac{\text{TeV}}{\text{cm}^2\text{s}}\right)$
Flux limit $\Phi_{90\%}$	$n_s = 38.95 \left(\hat{=} 6.74 \cdot 10^{-12} \frac{\text{TeV}}{\text{cm}^2\text{s}}\right)$	$n_s = 37.6 \left(\hat{=} 6.54 \cdot 10^{-12} \frac{\text{TeV}}{\text{cm}^2\text{s}}\right)$
P-value	0.8171	0.8261

Table 4: Stacking: Results for Sensitivity, discovery potential and flux limit $\Phi_{90\%}$ for \mathcal{TS} value stacking and p-value stacking. The p-value stacking is slightly more sensitive. The flux limit equals the sensitivity in both cases because the stacked \mathcal{TS} and $-\log_{10}p$ values are lower than the respective BG median.

Comparison

As described above the \mathcal{TS} value stacking and the p-value stacking do not necessarily have the same meaning. The \mathcal{TS} value is only directly comparable if positions with the same properties are considered. This means especially the same level of background fluctuations for each position. If this condition is not given, the \mathcal{TS} value stacking introduces a bias because the \mathcal{TS} value is not directly proportional to the signal probability anymore. This is because positions with high BG fluctuations get weighted stronger while positions with low fluctuations but a potentially higher signal remain underrepresented. The p-value stacking instead uses the background probability as stacking parameter. This is not anymore dependent on the background properties. Therefore it is an adequate method to stack also different objects. If on the other hand the source candidates show the same properties the \mathcal{TS} values of every position are comparable. Then the \mathcal{TS} value stacking is precise and a more straight forward way than the p-value stacking.

In this work positions with very different error region sizes are investigated and the background fluctuations differ considerably. This effect can be compensated by using the p-value stacking instead of the \mathcal{TS} value stacking. Therefore the results of the p-value stacking should be used as a reference.

5.3 Variation of considered error region

As explained in chapter 4.1 the exact shape of the reconstructed 90% error regions was not accessible. Therefore an elliptic approximation has been used what lead to the results presented above. Because the elliptic error region shape is an assumed approximation, the analysis has been repeated with the rectangular error region shape confined by the 90% restrictions on right ascension and declination without the elliptic cut.

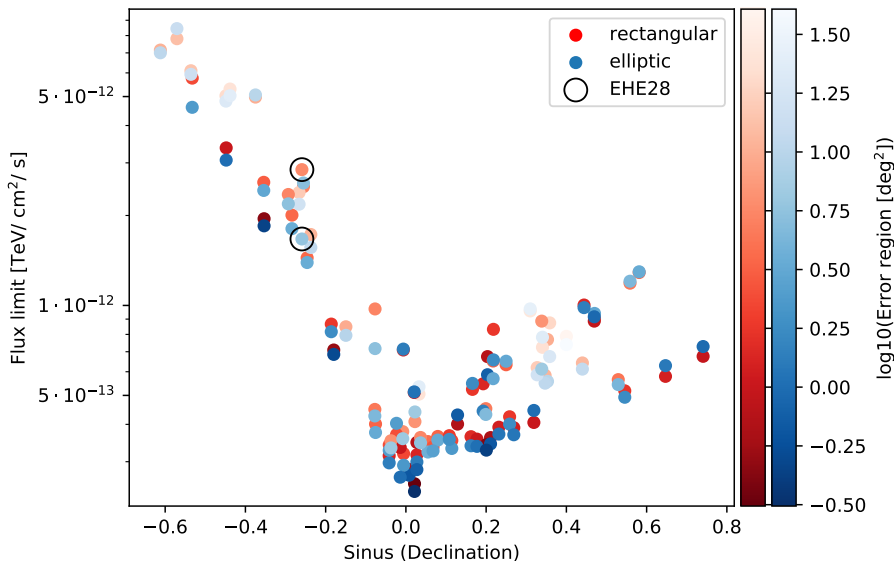


Figure 5.7: Comparison of results for flux limit $\Phi_{90\%}$ using the elliptic and the rectangular error region respectively. The results based on the rectangular approach (red) are in most cases slightly higher than the ones based on the elliptic approach (blue) due to higher background fluctuations. For some positions (e.g. EHE28, black circle) the flux limit is considerably higher when the rectangular region is considered. This could indicate that a possible source does not lie in the approximated elliptic region. Positions with larger error regions are indicated by whitened out dots.

The comparison of the results for the upper flux limits $\Phi_{90\%}$ using the elliptic and the rectangular approach are presented in figure 5.7 in a qualitative way. It is visible that in most cases the limit using the rectangular approach (marked red) is slightly higher than when the elliptic shape is considered (marked blue). This is due to higher background fluctuations caused by the increased error region. In some cases the limit of the rectangular approach is considerably higher (e.g. EHE28, black circle). This could indicate that a possible source does not lie in the approximated 90% confidence ellipse but still in the rectangle. Increasing the error region could therefore be a method to investigate the alert positions in a more extensive way. This could despite the increasing background fluctuations lead to notably different results. This was to be expected because the analysis was performed only with 90% confidence on the error region. The results for the rectangular analysis are shown in table 5 for the positions that have a lower p-value using the increased rectangular

error region. The positions for which the p-value decreased about more than 0.1 are highlighted **bold**. For EHE28 (highlighted red) at ra 99.0° and dec −15.02° the p-value decreased from 0.987 to 0.147. The flux limit assuming the rectangular shape is $2.847\text{e-}12 \frac{\text{TeV}}{\text{cm}^2\text{s}}$.

Name	p-value elliptic	p-value rect.	$\Phi_{90\%, \text{ rect}} \left[\frac{\text{TeV}}{\text{cm}^2\text{s}} \right]$
AHES7	0.491	0.324	$7.689 \cdot 10^{-13}$
AHES11	0.89	0.717	$7.154 \cdot 10^{-12}$
AHES12	0.73	0.689	$2.005 \cdot 10^{-12}$
DIF2	0.156	0.12	$6.742 \cdot 10^{-13}$
DIF5	0.454	0.336	$8.743 \cdot 10^{-13}$
DIF12	0.612	0.549	$5.835 \cdot 10^{-13}$
DIF16	0.669	0.623	$6.195 \cdot 10^{-13}$
DIF17	0.838	0.499	$5.647 \cdot 10^{-13}$
DIF18	0.666	0.645	$3.164 \cdot 10^{-13}$
DIF28	0.596	0.59	$3.644 \cdot 10^{-13}$
DIF29	0.509	0.5	$3.613 \cdot 10^{-13}$
EHE1	0.356	0.244	$5.467 \cdot 10^{-13}$
EHE2	0.848	0.684	$2.827 \cdot 10^{-13}$
EHE5	0.1	0.03	$9.734 \cdot 10^{-13}$
EHE8	0.36	0.198	$8.862 \cdot 10^{-13}$
EHE9	0.595	0.581	$3.14 \cdot 10^{-13}$
EHE11	0.66	0.624	$4.515 \cdot 10^{-13}$
EHE13	0.479	0.376	$3.48 \cdot 10^{-13}$
EHE14	0.943	0.585	$5.179 \cdot 10^{-13}$
EHE16	0.875	0.796	$3.421 \cdot 10^{-13}$
EHE18	0.988	0.986	$3.666 \cdot 10^{-13}$
EHE22	0.86	0.854	$3.414 \cdot 10^{-13}$
EHE25	0.98	0.938	$3.193 \cdot 10^{-13}$
EHE26	0.538	0.377	$3.347 \cdot 10^{-13}$
EHE27	0.667	0.644	$4.241 \cdot 10^{-13}$
EHE28	0.987	0.147	$2.847 \cdot 10^{-12}$
AHES19	0.264	0.231	$6.516 \cdot 10^{-13}$
AHES21	0.641	0.523	$5.298 \cdot 10^{-12}$
AHES23	0.836	0.806	$3.526 \cdot 10^{-13}$
EHE31	0.694	0.689	$8.484 \cdot 10^{-13}$
AHES26	0.546	0.396	$5.763 \cdot 10^{-12}$
DIF34	0.154	0.079	$8.318 \cdot 10^{-13}$
AHES28	0.759	0.69	$1.951 \cdot 10^{-12}$

Table 5: Results where the rectangular region yields lower p-values than the elliptic region. The positions for which the p-value decreased about more than 0.1 compared to the elliptic analysis are highlighted **bold**. For EHE28 (highlighted red) the p-value decreased from 0.987 to 0.147.

5.4 Comparison to limits of source catalog

In [14] point-like neutrino source searches using ten years of IceCube data within a selected source catalog are presented. The source catalog contains neutrino emission candidates. It is a subsample of the Fermi-LAT 4FGL catalog. The selection criteria are explained in [14]. In figure 5.8 the results from [14] for the flux limits $\Phi_{90\%}$ depending on the declination of the source are shown (gray dots). They follow the same course as the flux limits calculated in this work (red stars). This shows on the one hand again the strong declination dependency of the flux limits $\Phi_{90\%}$. On the other hand it leads to the conclusion that the point-source analyses done in [14] and in this work yield comparable results even though they investigate very different types of candidates (actual objects considered as source candidates and positions where a specific candidate has yet to be discovered).

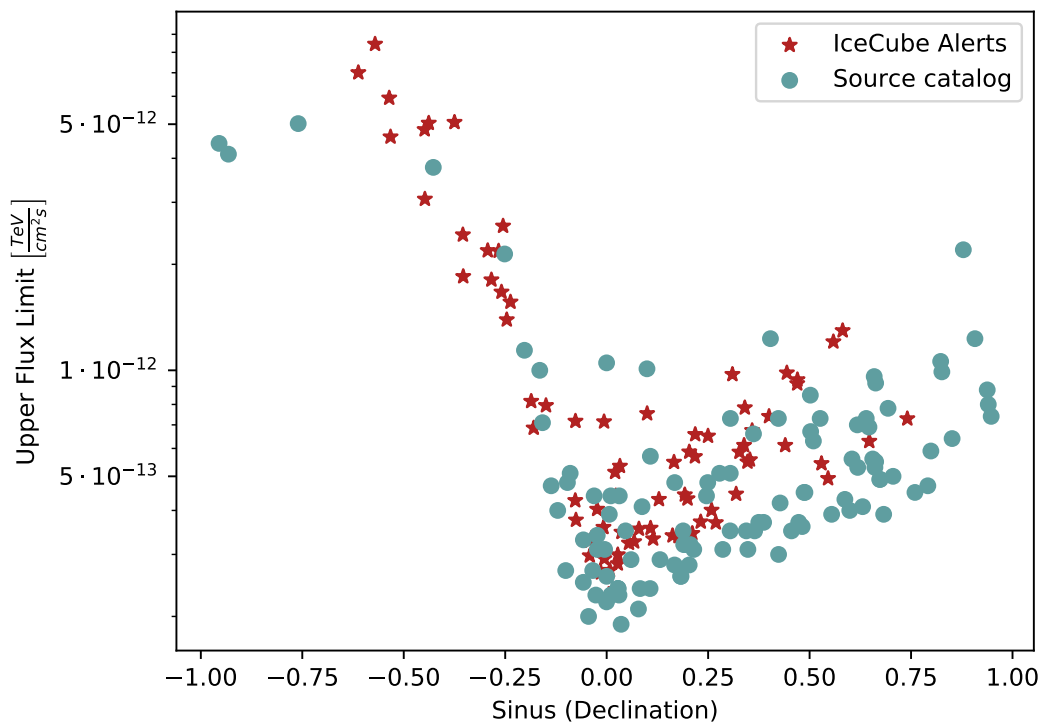


Figure 5.8: Comparison of limits $\Phi_{90\%}$ calculated in this analysis (red stars) to limits for a subsample of the Fermi-LAT 4FGL catalog (gray), described in [14]. Both follow the same course with a strong declination dependency.

6 Conclusion and outlook

The presented analysis yielded 13 candidate positions for which the 3σ discovery potential lies between the sensitivity and the flux limit $\Phi_{90\%}$. Therefor further investigations could lead to a discovery. This legitimates more expansive analyses of the alert positions and especially the 13 mentioned candidates. The most significant single source at ra 111.36° and dec -0.37° has a p-value of 0.022 and a flux limit of $7.144 \cdot 10^{-13} \frac{\text{TeV}}{\text{cm}^2\text{s}}$. All p-values have been calculated without trial correction.

The \mathcal{TS} value stacking results in a p-value of 0.8171 and the \mathcal{TS} stacked flux limit is constrained to $6.74 \cdot 10^{-12} \frac{\text{TeV}}{\text{cm}^2\text{s}}$. The p-value stacking results in a p-value of 0.8261 and the p-value stacked flux limit is constrained to $6.54 \cdot 10^{-12} \frac{\text{TeV}}{\text{cm}^2\text{s}}$. The stacking analysis did not measure any neutrino excess over background. A potential astrophysical signal from few sources is not visible if most of the stacked positions are only background. A possible adjustment would be to repeat the stacking analysis with exclusively the 13 mentioned candidate positions. The missing observation of an astrophysical signal could also emerge from very low astrophysical fluxes. A larger integration time is therefor necessary.

The individual analysis was performed separately for two types of error region shapes: Elliptical and rectangular. In few cases the flux limit was considerably higher when the point-source search was performed assuming the larger rectangular error region. This indicates that the actual source position does not always lie in the elliptic region. Therefor an analysis with increased error regions could pay off. For EHE28 at ra 99.0° and dec -15.02° the p-value decreased from 0.987 to 0.147 when the rectangular error region is used instead of the elliptic one. The flux limit $\Phi_{90\%}$ assuming the rectangular shape is $2.847 \cdot 10^{-12} \frac{\text{TeV}}{\text{cm}^2\text{s}}$ for this position.

The obtained results for $\Phi_{90\%}$ are compared to the ones obtained for a source catalog analyzed by the IceCube collaboration. The flux limits for both samples follow the same course depending on the declination.

The most promising method for further investigations is a *time-dependent* point-source search. This method considers not the whole IceCube data at once but divides it into smaller time windows. This makes the analysis also sensitive to *neutrino flares* which could be buried under the background of more than ten years of data in the performed analysis. This is very promising because the emission of blazars as one of the most promising currently considered neutrino source candidates is assumed to vary with time. The time-dependent analysis is already ongoing.

References

- [1] *IceCube South Pole Neutrino Observatory*, 07/2020. <https://icecube.wisc.edu>.
- [2] *IceCube Masterclass*, 07/27/2020. <https://masterclass.icecube.wisc.edu/en/learn/detecting-neutrinos>.
- [3] M. G. Aartsen et al. Improvement in fast particle track reconstruction with robust statistics, 2013. arXiv: 1308.5501.
- [4] Julia K. Becker. High-energy neutrinos in the context of multimessenger physics, 2007. arXiv: 0710.1557.
- [5] A. Boyarsky, M. Drewes, T. Lasserre, S. Mertens, and O. Ruchayskiy. Sterile neutrino dark matter, 2018. arXiv: 1807.07938.
- [6] IceCube Collaboration. Neutrino emission from the direction of the blazar txs 0506+056 prior to the icecube-170922a alert, 2018. arXiv: 1807.08794.
- [7] IceCube Collaboration, M. G. Aartsen, et al. Energy reconstruction methods in the icecube neutrino telescope, 2013. arXiv: 1311.4767.
- [8] IceCube Collaboration, M. G. Aartsen, et al. Evidence for high-energy extraterrestrial neutrinos at the icecube detector, 2013. arXiv: 1311.5238.
- [9] IceCube Collaboration, M. G. Aartsen, et al. All-sky search for time-integrated neutrino emission from astrophysical sources with 7 years of icecube data, 2016. arXiv: 1609.04981.
- [10] IceCube Collaboration, M. G. Aartsen, et al. The icecube neutrino observatory: Instrumentation and online systems, 2016. arXiv: 1612.05093.
- [11] IceCube Collaboration, M. G. Aartsen, et al. The icecube realtime alert system, 2016. arXiv: 1612.06028.
- [12] IceCube Collaboration, M. G. Aartsen, et al. Observation and characterization of a cosmic muon neutrino flux from the northern hemisphere using six years of icecube data, 2016. arXiv: 1607.08006.
- [13] IceCube Collaboration, M. G. Aartsen, et al. Measurement of the multi-TeV neutrino cross section with icecube using earth absorption, 2017. arXiv: 1711.08119.
- [14] IceCube Collaboration, M. G. Aartsen, et al. Time-integrated neutrino source searches with 10 years of icecube data, 2019. arXiv: 1910.08488.
- [15] The AMANDA Collaboration and J. Ahrens. Muon track reconstruction and data selection techniques in amanda, 2004. arXiv: astro-ph/0407044.

- [16] The IceCube Collaboration. The icecube data acquisition system: Signal capture, digitization, and timestamping, 2008. arXiv: 0810.4930.
- [17] Jacob Feintzeig. *Searches for Point-like Sources of Astrophysical Neutrinos with the IceCube Neutrino Observatory*. PhD thesis, University of Wisconsin-Madison, 2014.
- [18] J. A. Formaggio and G. P. Zeller. From ν_e to $\bar{\nu}_e$: Neutrino cross sections across energy scales, 2013. arXiv: 1305.7513.
- [19] Thomas K. Gaisser, Ralph Engel, and Elisa Resconi. *Cosmic rays and particle physics*. Cambridge University Press, 2016. ISBN: 978-0-521-01646-9.
- [20] David Griffiths. *Introduction to elementary particles*. VILEY-VCH, 2004. ISBN: 978-0-471-60386-3.
- [21] Francis Halzen and Dan Hooper. High-energy neutrino astronomy: The cosmic ray connection, 2002. arXiv: astro-ph/0204527.
- [22] Matthias Johannes Huber. Sensitivity studies for blazar stacking searches with the icecube neutrino observatory. Master's thesis, Technische Universität München, 2015.
- [23] Martina Karl. Search for neutrino emission in icecube archival data from the direction of icecube alert events, 2019. arXiv: 1908.05162.
- [24] Kai Michael Krings. *Search for Galactic and Extra-Galactic Neutrino Emission with IceCube*. PhD thesis, Technische Universität München, 2018.
- [25] Cecilia Lunardini, Gregory S. Vance, Kimberly L. Emig, and Rogier A. Windhorst. Are starburst galaxies a common source of high energy neutrinos and cosmic rays?, 2019. arXiv: 1902.09663.
- [26] Bogdan Povh et al. *Teilchen und Kerne*. Springer, 2014. ISBN: 978-3-642-37821-8.
- [27] Byron P. Roe, Hai-Jun Yang, Ji Zhu, Yong Liu, Ion Stancu, and Gordon McGregor. Boosted decision trees as an alternative to artificial neural networks for particle identification, 2004. arXiv: physics/0408124.
- [28] Biplob Sarkar. Active galactic nuclei (agn) and x-ray studies of galaxy m51. Master's thesis, 06 2011.
- [29] Christopher W. Walter. Experimental neutrino physics, 2008. arXiv: 0810.3937.